1   REVISION 1

2   **Mid-infrared emission spectroscopy and visible/near-infrared reflectance spectroscopy of**

3   **Fe-sulfate minerals**

4

5   Melissa D. Lane[1], Janice L. Bishop[2], M. Darby Dyar[3], Takahiro Hiroi[4], Stanley A. Mertzman[5],

6   David L. Bish[6], Penelope L. King[7], and A. Deanne Rogers[8]

7

8   [1]Planetary Science Institute, 1700 E. Fort Lowell Rd., Suite 106, Tucson, Arizona, U.S.A.

9   [2]SETI Institute/NASA-Ames Research Center, Mountain View, California, U.S.A.

10   [3]Mount Holyoke College, South Hadley, Massachusetts, U.S.A.

11   [4]Dept. of Geological Sciences, Brown University, Providence, Rhode Island, U.S.A.

12   [5]Department of Earth and Environment, Franklin and Marshall College, Lancaster, Pennsylvania,

13   U.S.A.

14   [6]Department of Geological Sciences, Indiana University, Bloomington, Indiana, U.S.A.

15   [7]Research School of Earth Sciences, Australian National University, Canberra, ACT, Australia

16   and Department of Earth Sciences, University of Western Ontario, London ON, Canada

17   [8]Department of Geosciences, State University of New York at Stony Brook, Stony Brook, New

18   York, U.S.A.

19

20

21

22   Email: lane@psi.edu

23

24   **Abstract**

25   Sulfate minerals are important indicators for aqueous geochemical environments. The

26   geology and mineralogy of Mars have been studied through the use of various remote-sensing

27   techniques, including thermal (mid-infrared) emission and visible/near-infrared reflectance

28   spectroscopies. Spectral analyses of spacecraft data (from orbital and landed missions) using

29   these techniques have indicated the presence of sulfate minerals on Mars, including Fe-rich

30   sulfates on the iron-rich planet. Each individual Fe-sulfate mineral can be used to constrain bulk

31   chemistry and lends more information about the specific formational environment (e.g., Fe^{2+}

32   sulfates are typically more water soluble than Fe^{3+} sulfates and their presence would imply a

33   water-limited (and lower Eh) environment; Fe^{3+} sulfates form over a range of hydration levels

34   and indicate further oxidation (biological or abiological) and increased acidification). To enable

35   better interpretation of past and future terrestrial or planetary data sets, with respect to the Fe-

36   sulfates, we present a comprehensive collection of mid-infrared thermal emission (2000 to 220

37   cm^{-1}; 5-45 μm) and visible/near-infrared (0.35-5 μm) spectra of 21 different ferrous- and ferric-

38   iron sulfate minerals. Mid-infrared vibrational modes (for SO_4, OH, H_2O) are assigned to each

39   thermal emissivity spectrum, and the electronic excitation and transfer bands and vibrational OH,

40   H_2O, and SO_4 overtone and combination bands are assigned to the visible/near-infrared

41   reflectance spectra. Presentation and characterization of these Fe-sulfate thermal emission and

42   visible/near-infrared reflectance spectra will enable the specific chemical environments to be

43   determined when individual Fe-sulfate minerals are identified.

44

45

46

47   Submitted to *American Mineralogist* on October 1, 2013.

48   Resubmitted on June 24, 2014.

49

50   Key words: mid-infrared, visible, near-infrared, spectroscopy, emissivity, reflectivity, sulfate,

51   spectra, reflectance, vibrational, iron, emission, reflectance

52

53   **1. Introduction**

54   The 370-390 sulfate-mineral species (Hawthorne et al., 2000; Athena Mineralogy URL,

55   http://athena.unige.ch/athena/mineral/minppcl6.html) are indicators of aqueous environments,

56   and can form over a broad range of geochemical conditions. Through evaluation of the chemical

57   formulae of these numerous sulfate species, we determined that approximately 25% of known

58   sulfate minerals are Fe-bearing (Fe^{3+}, Fe^{2+}). Fe^{3+} sulfate minerals tend to form in acidic

59   environments at a range of temperatures, through precipitation due to evaporation of

60   concentrated sulfuric acid solutions (e.g., H_2SO_4) such as may occur in volcanic

61   hydrothermal/fumarolic/aerosol or acid mine drainage environments; conversely, many Fe^{2+}

62   sulfates form at higher pH, in neutral to alkaline hydrothermal environments. Fe-bearing sulfates

63   occur not only on Earth, but there is strong evidence for Fe-bearing sulfates occurring on Mars as

64   well (e.g., Burns 1987). Fe^{2+} sulfates that form in a less oxidizing environment have been

65   identified on Mars, and there is a great likelihood that szomolnokite (and/or other Fe^{2+} sulfates)

66   (Bishop et al. 2009; Weitz et al. 2012) would be widespread because the martian environment is

67   enriched in iron and sulfur (specifically dominated by Fe^{2+}-bearing primary igneous minerals and

68   sulfate). There is visible/near-infrared (VNIR) spectral evidence for a broad distribution of the

69   similarly structured mono-hydrated sulfate species, kieserite, which is in solid solution with

70   szomolnokite (e.g., Arvidson et al. 2005; Gendrin et al. 2005; Bishop et al. 2009; Murchie et al.

71   2009; Roach et al. 2009). Fe^{3+} sulfates also have been identified on Mars as jarosite in the Ca-,

72   Mg-sulfate outcrops in Terra Meridiani using Mössbauer spectroscopy (Klingelhofer et al. 2004;

73   Morris et al. 2006), and as ferricopiapite, fibroferrite, hydronium jarosite, (para)butlerite;

74   (para)coquimbite, rhomboclase, or yavapaiite in yellowish/whitish light-toned soils in Gusev

75   Crater using VNIR and thermal infrared (TIR) spectroscopy (Johnson et al. 2007; Lane et al.

4

76   2008; Wang and Ling 2011). These light-toned soils were exposed serendipitously in the *Spirit*

77   rover tracks by a broken, dragging wheel (Figure 1) and may be extensive across Mars, although

78   buried in subsurface materials. The fine-grained dust on Mars also may contain hydrous Fe-

79   bearing sulfate minerals (Lane et al. 2004; Bishop et al. 2005) that could act as agents for

80   cementing the particles in the martian duricrusts (Binder et al. 1977; Mutch et al. 1977; Jakosky

81   and Christensen 1986).

82   Within the Fe-bearing subgroup of the almost 400 terrestrial sulfates, we determined the

83   majority (~87%) are hydrated with OH (~10%), H_2O (~44%), or both (~33%). Hence, these Fe-

84   bearing sulfates, along with other hydrated minerals, may host the H_2O that has been identified at

85   low and middle latitudes through measurement of hydrogen by the Gamma Ray Spectrometer

86   (GRS) and the Neutron Spectrometer (NS) that were flown on the Mars Odyssey spacecraft

87   (Boynton et al. 2002; Feldman et al. 2002, 2004; Bish et al, 2003; Wang et al. 2008;

88   Karunatillake et al., 2012). Hydrated Fe-sulfates can hold up to 50 wt.% H_2O in their structures.

89   On Mars, the close association of H_2O and S, and the H_2O:S molar ratio (between 2.4 and 4.0)

90   for 80% of the martian mid-latitudes (bulk regolith to decimeter depths) can be explained more

91   simply by the presence of Fe-sulfates rather than by Ca- or Mg-sulfates or other mineral phases

92   such as phyllosilicates or zeolites, thus affirming the importance and potential of Fe sulfates as a

93   hydrated mineral in the martian subsurface (Karunatillake et al., 2012, 2013).

94   Previously Lane (2007) published thermal infrared (TIR) (mid-infrared) emissivity

95   spectra of 37 various sulfates, only eight of which were Fe-bearing in their classical formulation.

96   Here we continue that work, with the objective of presenting thermal emissivity spectra (2000 to

97   220 cm^{-1}; 5 to 45 μm), as well as VNIR reflectance spectra (0.35-5 μm), of a larger suite of Fe-

98   bearing sulfates. This collection of Fe-sulfate spectra will permit better analyses of previously

5

99   acquired and future thermal emission and visible/near-infrared reflectance data, enabling a more

100   thorough understanding of the geology of Mars (as well as Earth and other planetary bodies

101   when similar remote-sensing techniques are utilized). The TIR and VNIR spectra presented in

102   this work are available as supplementary material to this paper in the Mineralogical Society of

103   America's online depository.

104

105   **2. Sample Descriptions**

106   For this study 21 iron-bearing sulfate mineral samples were studied (Table 1). These

107   include the mineral species amarantite, beaverite, botryogen-Zn, butlerite, copiapite/

108   ferricopiapite, coquimbite/paracoquimbite, goldichite, hydronium jarosite, jarosite, kornelite,

109   magnesiocopiapite, natrojarosite, parabutlerite, rhomboclase, römerite, rozenite, sideronatrite,

110   slavikite, szomolnokite, voltaite, and yavapaiite.

111   Many Fe sulfates occur together making spectral measurements on natural samples

112   difficult. To obtain the highest-quality, nominally one-phase laboratory spectra, the sulfate

113   mineral samples were coarsely crushed, hand-picked, and sieved in a best-attempt to purify the

114   sample, and then were analyzed by X-ray diffraction (XRD) to identify the mineral and any other

115   phases present. During the drawn-out collection and culling phase of the samples, various XRD

116   analyses were conducted at Franklin and Marshall College, Indiana University, and the

117   University of Western Ontario. These samples were also the subjects of a parallel Mössbauer

118   study (Dyar et al. 2014).

119   The hand-picked samples were sieved to particle sizes of <45 μm, 45-125 μm, and >125

120   μm (or 125-250 μm). Although all of the samples were measured by each technique, generally,

121   the TIR emissivity spectra of the coarsest samples are presented here in order to emphasize the

6

122   fundamental bands (i.e., increased spectral contrast) and minimize volume scattering effects

123   (e.g., Lyon 1964; Aronson et al. 1966; Hunt and Vincent 1968; Hunt and Logan 1972; Aronson

124   and Emslie 1973; Salisbury and Eastes 1985; Salisbury and Wald 1992; Moersch 1992; Hapke

125   1993; Moersch and Christensen 1995; Mustard and Hays 1997; Lane 1999) . The coarsest

126   particle-size sample was used unless a high-quality, pure, single-mineral spectrum was obtained

127   from the solid hand sample (chips or chunks) prior to sieving and hand-picking, or a pressed

128   pellet was made from the finest particulate sample after the XRD and VNIR data were obtained.

129   Pellets were formed using a standard Carver hydraulic 13 mm press and die. Pressing the fine-

130   grained samples into optically thick pellets (discs) eliminated the volume scattering effects from

131   the spectra. Note that only sulfate powder was pressed into the pellets; no other substrate was

132   included (e.g., KBr that is used for a transmission technique using pellets). The VNIR reflectance

133   spectra of generally the finest-particle samples are presented because of their increased sample

134   reflectance and enhanced spectral features.

135

136   **3. Experimental Methods**

137   **Thermal Infrared Emission Spectroscopy:** The samples in this study were analyzed for

138   thermal emission at ambient pressure using Arizona State University's Mars Space Flight

139   Facility. The spectrometer used is a modified Nicolet Nexus 670 E.S.P. FT-IR interferometer

140   attached to an external glove box containing a temperature-stabilized sample chamber

141   (maintained with circulating water behind the chamber wall). It is equipped with a

142   thermoelectrically stabilized deuterated triglycine sulfate (DTGS) detector and a CsI beam

143   splitter that allow the measurement of emitted radiation over the mid-infrared range of 2000 to

144   220 cm^{-1} (5 to 45 μm). To reduce and maintain the amount of atmospheric H_2O and CO_2 vapor

145   inside the spectrometer, external sample chamber, and glove box (and to reduce the degradation

146   of the hydrophilic CsI beam splitter) the entire system is continuously purged with air scrubbed

147   of H_2O and CO_2.

148   Each sample in a sample cup was placed into the sample chamber of the spectrometer and

149   heated to a sustained temperature, on average, of 50 ºC to minimize the loss of structural H_2O

150   and maintain the sulfate coordination. The samples were kept warm by actively heating the

151   sample cups during the data acquisition period of 160 or 270 scans at 2 cm^{-1} sampling while their

152   passively emitted radiation was measured. Each sample was measured several times and spectra

153   were summed for better signal-to-noise and to produce a representative average spectrum.

154   Additional details of the data calibration are presented in Christensen and Harrison (1993),

155   Wenrich and Christensen (1996), and Ruff et al. (1997).

156

157   **Visible, Near Infrared Reflectance Spectroscopy:** Reflectance spectra were acquired at

158   Brown University's RELAB facility. Bidirectional spectra were collected for the samples relative

159   to halon using a VNIR spectrometer from 0.3 to 2.5 μm at 5 nm spectral sampling under ambient

160   conditions using a standard configuration (incidence = 30°; emission = 0°), then corrected for the

161   absolute reflectance of the halon. Additional reflectance spectra were measured from 1-50 μm

162   using a biconical Nicolet FTIR spectrometer in a controlled, dry environment relative to a rough

163   gold surface as in previous studies (Bishop and Murad 2005). The infrared spectra were

164   measured with 2 cm^{-1} spectral sampling in an environment purged of H_2O and CO_2 for 10-12

165   hours. Composite, absolute reflectance spectra were prepared by scaling the FTIR data to the

166   bidirectional data near 1.2 μm.

167

8

168   **4. Obtained Spectra and Assignment of the Bands**

169   **TIR Emissivity Data:** Sulfate minerals may be distinguished using thermal infrared

170   (mid-infrared) spectroscopy because each crystal structure and specific chemical composition

171   produce a distinct spectrum as a result of the fundamental vibrational modes of the crystal

172   structure and their associated overtones and combination bands. Mid-infrared sulfate mineral

173   spectra are dominated by the vibrational behavior of the S-O bonds in the sulfate anion, and in

174   some cases, influenced by the presence of OH or H_2O, or even CO_3, in the structure. Early mid-

175   infrared spectroscopic studies showed that the aqueous sulfate anion (SO_4^{2-}) produces four

176   infrared absorption features at ~1105, ~983, ~611, and ~450 cm^{-1} corresponding to the

177   asymmetric stretch, v_3; symmetric stretch, v_1; asymmetric bend, v_4; symmetric bend, v_2,

178   respectively (Nakamoto 1986; also see Herzberg 1945; Hug 1997), of which only v_3 and v_4 are

179   infrared active. These vibrations are modified from simple T_d site symmetry when the sulfate

180   anion is present within a solid-state medium, such as a mineral with a repeating molecular

181   structure. Cation complexation of SO_4^{2-} causes distortions of the sulfate polyhedra (e.g., Griffen

182   and Ribbe 1979), resulting in the potential appearance of all four sulfate vibrational modes (i.e.,

183   band splitting / removal of degeneracy) in the spectrum due to lowered symmetry (e.g., Ross

184   1962; Steger and Schmidt 1964; Hezel and Ross 1966; Brown and Ross 1970; Chio et al 2004;

185   Makreski et al. 2005; Lane 2007; Majzlan and Michallik 2007; Hyde et al. 2011; Apopei et al.

186   2012). In a solid-state sulfate mineral, internal vibrational features generally appear at ~1050-

187   1250 (v_3), ~1000 (v_1), ~500-700 (v_4), and ~400-500 (v_2) cm^{-1} (e.g., Herzberg 1945; Nakamoto

188   1986; Vassallo and Finnie 1992; Bishop and Murad 2005; Lane 2007; Hyde et al. 2011), and at ~

189   <550 cm^{-1} due to lattice vibrations (e.g., Serna et al. 1986; Clark 1999; Lane 2007), including

190   metal-oxygen, librational and translational modes that occur at lower wavenumbers, respectively.

9

191   The ν_2 band is known to be significantly weaker than the ν_1 mode and commonly is not

192   observable in the infrared spectra of sulfates (Hezel and Ross 1966). Additional bands may

193   appear in the emissivity spectra due to the presence of H_2O or hydroxyl in the crystal structure.

194   These features include H_2O bending (δH_2O) modes (Omori and Kerr 1963; Ross 1974), and

195   metal-OH in-plane (δ) and out-of-plane (γ) bending modes (e.g., Libowitzky 1999; Majzlan et al.

196   2011). Note that the spectral band positions mentioned above and presented in this work are the

197   locations of the features on the emissivity spectra, not the frequencies of oscillators used in

198   dispersion theory.

199   Most sulfate minerals consist of SO_4 tetrahedra polymerized to various degrees with MO_6

200   polyhedra (where M is a cation), providing an organizational basis for the crystal structure

201   descriptions in Hawthorne et al. (2000). Their structural organization is borrowed for this paper

202   as well.

203

204   **VNIR Reflectance Data:** Early reflectance spectra of sulfates in the VNIR region

205   demonstrated that the dominant bands near 1.4-1.5 and 1.9-2.0 μm are due to H_2O (Hunt et al.

206   1971). More recent VNIR studies covered additional sulfate minerals and showed that both OH

207   and H_2O are responsible for most features in the 1-3 μm range (e.g., Clark et al. 1990; Crowley

208   1991; Bishop and Murad 1996; Bishop and Murad 2005; Cloutis et al. 2006; Hyde et al. 2011);

209   however, features near 4.3-5.3 μm are attributed to overtones and combinations of the ν_3 SO_4

210   vibration (Blaney and McCord 1995; Bishop and Murad 2005; Hyde et al. 2011). VNIR

211   reflectance spectra have been presented in recent studies for some Fe sulfates but spectra of

212   many of these cover only the spectral range of 0.4-2.5 μm and the hydration state of the sample

213   was not always certain: rozenite, rhomboclase, voltaite, halotrichite, coquimbite/paracoquimbite,

10

214   copiapite/ferricopiapite, amarantite, jarosite, fibroferrite, sideronatrite, botryogen, and

215   szomolnokite (Crowley et al. 2003; Lane et al. 2004; Bishop and Murad 2005; Bishop et al.

216   2005; Cloutis et al. 2006). The current study presents VNIR reflectance spectra, coordinated with

217   the mid-IR data and mineral structure, for high-purity and well-characterized samples.

218   Schwertmannite is often classified as a sulfate mineral, but is actually an Fe oxyhydroxide

219   mineral similar to akaganeite (Bigham et al. 1994) and is not included in this study.

220   Schwertmannite has sulfate groups present as anions inside the structural tunnels and exhibits

221   spectral properties similar to ferrihydrite (Bishop and Murad 1996).

222   Optical absorption bands are observed from 0.4 to ~1.2 µm for Fe-bearing sulfate

223   minerals (Burns 1993). Many Fe sulfates exhibit a sharp but weak band near 0.43 µm due to the

224     $^6A_{1g}$ to ($^4A_{1g}$, ^4E_g) electronic excitation transition (Crowley et al. 2003; Bishop and Murad 2005;

225   Cloutis et al. 2006). An additional electronic band occurs near 0.5-0.6 µm in many Fe sulfate

226   spectra due to the $^6A_{1g}$ to $^4T_{2g}$ transition that generally results in a shoulder in VNIR reflectance

227   spectra but is occasionally observed as a band (Crowley et al. 2003; Bishop and Murad 2005;

228   Cloutis et al. 2006). The $^6A_{1g}$ to $^4T_{1g}$ electronic transition can occur over a wider wavelength

229   range, from ~0.77 to 0.93 µm (Crowley et al. 2003; Bishop et al. 2005; Bishop and Murad 2005;

230   Cloutis et al. 2006). The Fe^{2+} crystal field band occurs at longer wavelengths, near 0.9-1.2 µm

231   (Burns 1993; Cloutis et al. 2006).

232

233   **4.1. Finite Clusters of SO$_4$ Tetrahedra and MX_6 Octahedra**

234   The minerals in this structure group (Figures 2a, b) are comprised of finite clusters of SO$_4$

235   tetrahedra and MX_6 octahedra, where X is an unspecified ligand (such as H$_2$O or OH), and the

236   structural groups are linked through hydrogen bonding (see Hawthorne 1985).

11

237   **Coquimbite/paracoquimbite:** The structures of coquimbite and its polytype

238   paracoquimbite are based on layers of $[Fe_3(SO_4)_6]$ clusters (whose long axis is parallel to [001]),

239   isolated $\{Fe(H_2O)_6\}$ octahedra, and H_2O groups. The $Fe(H_2O)_6$ octahedra are connected into

240   sheets by hydrogen bonding. The coquimbite/paracoquimbite sample studied here is well

241   crystalline and contains approximately subequal amounts of the two minerals as determined by

242   XRD. The sample spectrum (Figure 2a) shows two clear ν_3 features at 1180 and 1100 cm^{-1}; the

243   shape of the 1100-cm^{-1} band suggests that there may be another weaker ν_3 band at slightly lower

244   frequency, in contrast to the three bands seen in the transmission data of Moenke (1962 as

245   reported by Ross 1974). A strong ν_1 feature is present at 1013 cm^{-1}. Three ν_4 bands occur at 685,

246   650, and 597 cm^{-1}; however, the 685-cm^{-1} band is very small but distinct in this very clean

247   spectrum. The ν_2 features occur at 480 and 443 cm^{-1} with strong lattice modes occurring at <350

248   cm^{-1}. The bands that result from the H_2O in the coquimbite structure can be seen at ~890 and 816

249   cm^{-1} (bending modes) and the δH_2O is seen subtly at 1690 cm^{-1}.

250   **Römerite:** Römerite contains Fe^{2+} that coordinates with six H_2O molecules and Fe^{3+} that

251   binds four H_2O molecules and two oxygen anions in different SO_4 groups. As such, the structure

252   of römerite is based also on isolated $\{Fe(H_2O)_6\}$ octahedra and $[Fe(SO_4)_2(H_2O)_4]_2$ groups that

253   are weakly connected by hydrogen bonding between the unconnected octahedral and within the

254   latter group (Fanfani et al. 1970; Hawthorne et al. 2000). In römerite (Figure 2a), the H_2O in the

255   structure appears as an emissivity maximum at ~1673 cm^{-1}. There are three clear ν_3 features

256   occurring at 1139, 1078, and 1035 cm^{-1} with another subtle shoulder bump that may be a

257   possible ν_3 at ~1168 cm^{-1}. A strong ν_1 feature occurs at 996 cm^{-1} and 2 possible ν_4 features can

258   be seen at ~658 and ~593 cm^{-1}. It is possible that a H_2O libration feature occurs as a small band

12

259 at 815 cm^{-1}. A ν_2 feature occurs at ~477 cm^{-1}. A strong lattice mode is present, but the band is

260 truncated on the long-wavelength side, so the position of its deepest point is unknown.

261 **Rozenite:** The structure of rozenite (ferrous iron only) is comprised of [Fe$_2$(SO$_4$)(H$_2$O)$_8$]

262 clusters that are solely hydrogen bonded together, both within and between the clusters

263 (Hawthorne et al, 2000). The H$_2$O in rozenite causes an emissivity maximum at ~1680 cm^{-1} (due

264 to the δH$_2$O mode), and a band at 818 cm^{-1} and weaker bands at ~760, 735, and ~692 cm^{-1} that

265 are attributed to δOH (Figure 2a). Rozenite exhibits a deep ν_3 feature at 1100 cm^{-1} and two small

266 shoulder features at ~1013 and ~1220 cm^{-1} that also are representative of the ν_3 bands. The ν_1

267 band appears at 992 cm^{-1}. The rozenite spectrum shows a fairly broad ν_4 band centered at ~602

268 cm^{-1} with two other ν_4 bands that appear as subtle shoulders on the higher frequency side at ~660

269 and ~645 cm^{-1}, and a possible ν_2 band at ~468 cm^{-1}.

270

271 **VNIR Reflectance Data:** The coquimbite spectrum exhibits three Fe^{3+} excitational

272 absorptions at 0.43, 0.56, and 0.78 µm (similar to bands observed for coquimbite by Bishop et al.

273 2005 and Cloutis et al. 2006), while the rozenite spectrum has a sharp band at 0.43 µm and a

274 broad Fe^{2+} excitational absorption centered near 1.0 µm with a shoulder near 1.2 µm (similar to

275 features seen by Crowley et al. 2003 and Bishop et al. 2005). The römerite spectrum contains a

276 shoulder near 0.5 µm, Fe^{3+} bands near 0.85 and 0.91 µm with a broad shoulder out to ~1.17 µm

277 due to Fe^{2+} (Figure 2b).

278 The coquimbite and römerite spectra have similar NIR vibrational bands; both include a

279 weak band/shoulder at 1.45 µm and a weak band at ~1.78 µm. A strong H$_2$O doublet, due to

280 stretching plus bending combination vibrations, is found at 1.93 and 2.01 µm for römerite and

281 1.94 and 1.98 µm for coquimbite. A shoulder feature due to H$_2$O is found near 2.55 µm for

13

282   römerite, and the H_2O stretching vibration occurs near 2.75-3 µm. A doublet near 2.49 and 2.57

283   µm is observed in coquimbite, along with a strong H_2O stretching vibration near 2.9-3.1 µm that

284   has completely saturated the spectrum. The rozenite spectrum exhibits H_2O overtone and

285   combination bands centered at 1.4 and 1.9 µm, respectively. A doublet is observed at 2.42 and

286   2.53 µm, a strong broad H_2O stretching vibration is seen from 2.9-3.2 µm, and a set of SO_4

287   overtones and combinations occurs from 4.2-4.9 µm.

288

289   **4.3. Infinite chains of SO_4 tetrahedra and MX_6 octahedra**

290   The minerals in this structure group (Figures 3a-e) are comprised of infinite chains of

291   SO_4 tetrahedra and MX_6 octahedra, and the chains often are parallel to the c axis of the mineral

292   (see Hawthorne, 1985).

293   **Amarantite:** The amarantite structure is based on two octahedra that edge-share (a

294   dimer) with an additional two octahedra that attach to the dimer, making a tetramer (Figure 3a).

295   Further, two sulfate tetrahedra attach to this tetramer to form a $[Fe_2O(H_2O)_4(SO_4)_2]$ chain and

296   provide additional linkages to other tetramers comprising more complex chains (Süsse 1968;

297   Hawthorne et al. 2000). With the additional H_2O, the amarantite formula may be written as

298     $[Fe_2O(H_2O)_4(SO_4)_2](H_2O)_3$.

299   The emissivity spectrum of amarantite is shown in (Figure 3a). The bending mode of the

300   H_2O in the structure is seen at ~1642 cm^{-1}, whereas asymmetric SO_4 stretching modes occur at

301   ~1215 (as a shoulder), 1154, 1090, and 1059 cm^{-1}. There is a small doublet in the spectrum that

302   may represent both the δOH mode at 1018 cm^{-1} and the v_1 band at 1004 cm^{-1}. However, if the

303   doublet is really just jagged due to noise, then the middle of that band would be at ~1009 cm^{-1}

304   and would likely represent just the v_1 band. Other features include two small bands at 804 and

14

305    $\sim$748 cm^{-1} for the δOH modes; ν_4 modes occur at $\sim$645, 595, and $\sim$528 cm^{-1}; the ν_2 mode band is

306   at 463 cm^{-1}. A long-wavelength band is present at $\sim$289 cm^{-1} as well as a truncated band.

307   **Botryogen-Zn:** In botryogen, the infinite chains of Fe-centered octahedra are linked to

308   SO$_4$ tetrahedra, to which Zn-centered octahedra attach through one of the tetrahedral vertices

309   (Figure 3a). This structure is represented as [ZnFe(OH)(H$_2$O)$_6$(SO$_4$)$_2$](H$_2$O). Interchain linkages

310   are present exclusively through hydrogen bonding (Hawthorne 1985; Hawthorne et al. 2000).

311   The botryogen-Zn emissivity spectrum (Figure 3a) has many bands for this complex, monoclinic

312   salt, due to the presence of OH and H$_2$O in the structure and its low symmetry. The ν_3 bands

313   occur at 1220, 1132, and 1031 cm^{-1} with additional ν_3 bands at 1164 (shoulder) and 1068 cm^{-1}.

314   These five ν_3 bands exhibited in zincobotryogen are comparable to the five ν_3 bands shown for

315   botryogen in the transmission data of Moenke (1962) as assigned by Ross (1974). The ν_1 band is

316   small but clear at 999 cm^{-1}. It is possible that the small band at 1010 cm^{-1} is due to H$_2$O in the

317   mineral (δOH) because it occurs just to the high-frequency side of the ν_1 band, similar to the

318   same band relationship in jarosite to be discussed below. A small feature at 805 cm^{-1} also could

319   result from an OH bending vibration. Constituent H$_2$O additionally causes a bending mode

320   (δH$_2$O) to be seen at 1660 cm^{-1} (Ross 1974). Three strong ν_4 bands are present at 602, 545, and

321   485 cm^{-1}, with a broad, less-defined band at $\sim$655 cm^{-1}. The ν_2 band may occur at $\sim$393 cm^{-1} and

322   there is a strong lattice band at $\sim$280 cm^{-1}.

323   **Butlerite/parabutlerite:** In butlerite/parabutlerite, infinite chains of

324   [Fe(OH)(H$_2$O)$_2$(SO$_4$)] are linked solely by hydrogen bonding, and there are no interstitial cations

325   (Hawthorne et al. 2000) (Figure 4a). In the butlerite spectrum (Figure 3a), the H$_2$O in the

326   structure appears as an emissivity maximum at $\sim$1688 cm^{-1}. There is a clear ν_3 feature at 1123

327   cm^{-1} with other subtle ν_3 shoulder bumps at $\sim$1200 and $\sim$1045 cm^{-1}; the ν_1 feature occurs at 992

15

328   cm^{-1}. The bands at 1013 and 806 cm^{-1} are due likely to δOH modes. Four ν_4 features can be seen

329   at 694, 657, 592, and 506 cm^{-1}. The bands at 441 and ~413 may be ν_2 bands, and there is a strong

330   lattice band at ~252 cm^{-1} but the noise in the data confuses the position and it may be a truncated

331   band whose true position is masked by the jaggedness of the spectrum at the lower

332   wavenumbers. The spectrum of the parabutlerite sample (Figure 3a) is very similar to that of

333   butlerite and offers an example of sample-to-sample variations that may arise in the spectra. As

334   in butlerite, for parabutlerite the H_2O deformation mode occurs at ~1688 cm^{-1} and the δOH mode

335   at 1013 cm^{-1}. The ν_3 features occur at 1233, 1176, 1098, 1054, and 1024 cm^{-1} and the ν_1 mode is

336   found at 997 cm^{-1}. Other bands seen at 650, 602, 503, and ~476 cm^{-1} represent the ν_4 modes.

337   Bands at 446 and ~330 cm^{-1} may be ν_2 modes and lattice modes may occur at ~256 cm^{-1} and as a

338   deep, but truncated, band.

339   **Copiapite/ferricopiapite and Magnesiocopiapite:** Majzlan and Michallik (2007)

340   describe the structure of the copiapite group minerals as a combination of infinite chains of

341    $[Fe_4(SO_4)_6(H_2O)_8(OH)_2](H_2O)_2$ and slabs of $\{[M(H_2O)_6](H_2O)_4\}$, where M is Fe^{3+} in copiapite

342   and Mg^{2+} in magnesiocopiapite. The charge difference requires subtle structural variations.

343   Emissivity spectra of copiapite and magnesiocopiapite are shown in Figure 3a, and it can be seen

344   that their spectra are quite similar. The largest difference occurs because the magnesiocopiapite

345   sample was measured as a pressed pellet, whose resulting spectrum was less noisy, with deeper

346   spectral features than the copiapite spectrum. Also, the magnesiocopiapite spectrum shows a

347   distinct δOH band that is not evident in the copiapite spectrum (except perhaps as a subtle

348   shoulder on the ν_1 band).

349   Specifically, the copiapite spectrum exhibits ν_3 bands at ~1212, ~1109, and 1047 cm^{-1}.

350   The ν_1 clearly occurs at 998 cm^{-1}. The ν_4 bands are found at ~603 and ~542 cm^{-1}. The ν_2 band is

16

351   exhibited at ~410 cm^{-1} and a strong lattice mode is truncated so its actual position is unclear. The

352   δH_2O and δOH features are seen at ~1662 and ~790 cm^{-1}, respectively. In magnesiocopiapite,

353   the bands are as follows: the H_2O deformation mode (δH_2O) occurs at ~1656 cm^{-1}, the ν_3 bands

354   are at 1213, 1146 (a shoulder), 1107, 1049, and possibly a shoulder at 1031 cm^{-1}. The ν_1 band is

355   found at 997 cm^{-1} with a distinct δOH feature at 1013 cm^{-1}. Three ν_4 bands are seen at 639, 595,

356   and 556 cm^{-1}, and a ν_2 band is present at 414 cm^{-1}. A final band may occur at ~262 cm^{-1};

357   however, this band may be affected by noise and is also truncated so its position is uncertain.

358   **Sideronatrite:** This mineral species is based on infinite octahedral-tetrahedral chains that

359   show considerable disorder in relation to the adjacent chains in their structure (Figure 3a). The

360   backbone structure consists of infinite chains of $[Fe(SO_4)_2(OH)]^{2-}$ that align parallel to the *c* axis

361   (Scordari and Ventruti 2009; Scordari et al. 2010; Della Ventura et al. 2013) that are crosslinked

362   by Na-distorted octahedra in which each Na atom is linked to four oxygen atoms and two H_2O.

363   Hydrogen bonding to the infinite chains is provided through these water molecules. The

364   sideronatrite crystal structure and thermal emissivity spectrum of this pelletized sample are

365   shown in Figure 3a. The pelletized sample produced a clean spectrum that shows the H_2O

366   deformation mode as an emissivity minimum at ~1637 cm^{-1}. Many ν_3 features are apparent,

367   including those at 1270 (small), 1217, 1208, 1139, 1112 (shoulder), 1068, and 1034 cm^{-1}. A

368   sharp ν_1 feature occurs at 997 cm^{-1}; however, this deep feature's shape indicates that a δOH

369   feature may be overlapping, or that this is the primary δOH feature and a ν_1 may be overlapping;

370   Della Ventura et al. (2013) identify two bands here at 997 and 981 cm^{-1} but assign them both to a

371   ν_1 splitting. Other distinct features (representing ν_4) are found at 666, 650, 634, 620, 609, and a

372   very deep band at 519 cm^{-1}; Della Ventura et al. (2013) attribute this band to ν_2. This deep band

373   alternatively may be assigned to γOH. Bands at 409 and 400 cm^{-1} represent ν_2 modes, and the

17

374   lowest wavenumber bands (typically metal-oxygen or lattice modes) are seen at 308 and ~265

375   cm^{-1} and a deep, truncated band.

376

377   **VNIR Reflectance Data:** The amarantite spectrum contains an Fe^{3+} excitation at 0.87

378   µm that is also seen in botryogen at 0.93 µm, and in butlerite/parabutlerite at 0.92 µm (Figure

379   3b). Copiapite and Mg-copiapite spectra both have an Fe^{3+} band at 0.88 µm that also occurs in

380   the sideronatrite spectrum at 0.94 µm (Figure 3c).

381   There are numerous narrow NIR bands in sideronatrite that are attributed to H_2O and OH

382   near 1.45, 1.91, 1.99, 2.27, 2.5, 2.8, and 2.95 µm. Additional bands in the 4-5 µm region are

383   consistent with overtones and combinations of the SO_4 vibrations (Figure 3c). The many doublet

384   and triplet features observed in the sideronatrite spectrum indicate that these bands have been

385   split, probably due to multiple H_2O and OH sites in the mineral structure. Similar features were

386   observed in sideronatrite spectra by Cloutis et al. (2006). The NIR spectra of amarantite,

387   botryogen, and copiapite all exhibit H_2O bands near 1.45, 1.95, and 2.8-3.2 µm. The H_2O

388   stretching overtone near 1.4 µm and combination band near 1.9 µm both occur as a doublet for

389   amarantite, botryogen, butlerite, and parabutlerite: at 1.447 and 1.478, and at 1.944 and ~1.98

390   µm in spectra of amarantite (related to those observed by Cloutis et al. 2006), at 1.447 and 1.480,

391   and at 1.929 and 1.960 µm in spectra of botryogen (similar to those observed by Cloutis et al.

392   2006), at 1.476 and 1.503, and at 1.960 and 2.026 µm in spectra of butlerite, and at ~1.48 and

393   ~1.50, and at 1.961 and ~2.03 µm in spectra of parabutlerite. The butlerite and parabutlerite also

394   have OH combination stretching plus bending vibrations at 2.24 and 2.28 µm (Figure 3b). Each

395   of these spectra includes SO_4 overtones and combinations over the range ~4.2-4.8 µm.

18

396   Shown in Figures 3d,e are examples of spectra of three particle sizes of the amarantite

397   and botryogen samples, respectively. The spectral brightness in the VNIR region is brighter for

398   the finer particle-size samples and there are some differences in band depth, but no changes are

399   evident in the band center. For this paper we are focusing on the band centers and, hence, are

400   presenting only the VNIR reflectance spectra of the fine particle-size fractions.

401

402   **4.4. Infinite sheets of $M_3(OH)_6(SO_4)_2$**

403   The minerals in this structure group (Figures 4a, b) are comprised of infinite

404    $[M_3(OH)_6(SO_4)_2]$ sheets.

405   **Beaverite:** The rhombohedral structure of beaverite (Figure 4a) consists of tetrahedral-

406   octahedral-tetrahedral sheets that lie perpendicular to the c axis. The Fe-centered octahedra are

407   linked along the sheet with OH groups. The two remaining OH-attached vertices along the c axis

408   connect the octahedral layer to sheets of SO_4 tetrahedra that also lie perpendicular to the c axis.

409   Beaverite is a member of the alunite-jarosite group (Breidenstein et al. 1992); however, its

410   spectrum (Figure 4a) is somewhat dissimilar to those of alunite or jarosite. This sample was

411   pelletized and produced a low-noise spectrum that shows the H_2O deformation mode as an

412   emissivity minimum at ~1602 cm^{-1}. The ν_3 bands are seen at 1163, 1110, and possibly 984 cm^{-1}.

413   The ν_1 occurs at 1001 cm^{-1} and there appears to be a δOH at 1019 cm^{-1}. An additional δOH is at

414   ~735 cm^{-1}. A strong ν_4 band is seen at 625 cm^{-1} with two smaller ν_4 bands at 604 and 575 cm^{-1}.

415   Following the spectral character of jarosite described in detail below, the beaverite spectrum

416   shows a ν_2 band at 423 cm^{-1}. Strong metal-oxygen lattice modes occur at 512 and 469 cm^{-1} and

417   another is seen as a large truncated band.

19

418   **Jarosite, Hydronium Jarosite, Natrojarosite:** The structure of the jarosite-group

419   minerals (Figure 4a) may be described as a series of layers formed by tetrahedral-octahedral-

420   tetrahedral sheets that lie perpendicular to the c axis. In the sheets made of Fe-centered

421   octahedra, the Fe atoms are linked through hydroxyl groups (Serna et al. 1986). The tetrahedral

422   (SO_4) sheets are joined by the cations (e.g., K in jarosite, H_3O in hydronium jarosite, and Na in

423   natrojarosite) that are found at the center of polyhedra surrounded by six oxygen atoms and six

424   OH groups) (Basciano and Peterson 2008). The mid-infrared spectra of jarosite, hydronium

425   jarosite, and natrojarosite are presented in Figure 4a. Their similar structures cause their

426   emissivity spectra to be remarkably similar as well.

427   The jarosite spectrum was taken of a solid jarosite coating on a host rock. The jarosite

428   emissivity spectrum exhibits two v_3 bands at 1220 and 1112 cm^{-1}, a v_1 band at 1006 cm^{-1}, and a

429   single v_2 at 445 cm^{-1}. This spectrum shows a subtle shoulder at ~662 cm^{-1} on a stronger feature at

430   635 cm^{-1} suggesting two v_4 bands. Additional modes of jarosite are shown to occur at ~1020

431   (due to δOH) and 524, 476, ~336, and ~242 cm^{-1} due to Fe-O lattice modes. The broader lattice-

432   mode band at 524 cm^{-1} suggests a possible superposed γOH mode on the higher frequency side

433   of the feature as observed by both Serna et al. (1986) and Sasaki et al. (1998). An emissivity

434   maximum at 1633 cm^{-1} results from δH_2O (e.g., Omori and Kerr 1963).

435   Hydronium jarosite differs from jarosite by the replacement of K^+ with H_3O^+ in its

436   structure. The hydronium jarosite analyzed in this study was not a pure endmember because

437   XRD peaks were shifted slightly, suggesting minor substitution of H_3O^+ by another cation (e.g.,

438   K^+ or Na^+). The hydronium jarosite spectrum is of much lower quality than the jarosite spectrum

439   (that was a well-formed coating on a host rock) or the natrojarosite spectrum (that was taken of a

440   pressed pellet). This noise makes the identification of the band position much less accurate;

20

441   however, the best determinations are as follows. The H_2O bending mode (δH_2O) is found at

442   ~1651 cm^{-1}, the asymmetric SO_4 stretching modes occur at ~1220 and 1121 cm^{-1}, the ν_1 band lies

443   at ~997 cm^{-1}, and the δOH band is shown at 1033 cm^{-1}. Three uncertain bands at 898, 845, and

444   ~760 cm^{-1} may represent additional δOH modes. The ν_4 modes occur at 675 and 635 cm^{-1}, and

445   the ν_2 mode bands are at 428 and 393 cm^{-1}. Other M-O or lattice modes occur at ~526, 475, and

446   ~336 cm^{-1}, and an additional long-wave band is present at ~265 cm^{-1} but that may just be the

447   local bottom of the feature due to noise and its true position is truncated.

448   Natrojarosite differs from jarosite by the replacement of K^+ with Na^+ in its structure. For

449   the natrojarosite sample, we measured a pressed pellet. The emissivity spectrum (Figure 4a) of

450   natrojarosite shows the H_2O deformation mode (δH_2O) to occur at ~1635 cm^{-1} (e.g., Omori and

451   Kerr 1963); the ν_3 bands are seen at 1200 and 1107 cm^{-1}. The small ν_1 band occurs at ~1010 cm^{-1}

452   and a δOH feature is found at 1026 cm^{-1}. Two ν_4 bands are seen at ~666 and 632 cm^{-1}, and a ν_2

453   band is present at 441 cm^{-1}. Other distinct bands occur at 524, 478, and 327 cm^{-1} with a possible

454   additional band at 347 cm^{-1}. A large truncated band also is apparent in the spectrum.

455   Spectral comparison shows the positions of the bands in all of the jarosite-group minerals

456   to be generally similar (Figure 4a; Table 2), with a few notable exceptions. In natrojarosite, the

457   ν_4 bands are split more broadly than for jarosite, which exhibits only a single feature with a

458   shoulder (Lane 2007). The same bands in hydronium jarosite are spaced even farther apart. Also,

459   the ν_2 feature in natrojarosite is at just slightly lower frequency than in jarosite, but the ν_2 feature

460   in hydronium jarosite occurs at ~15 cm^{-1} lower wavenumber than in the other two jarosite-group

461   minerals.

462

21

463   **VNIR Reflectance Data:** Crystal field bands are observed for the jarosite type minerals

464   near 0.43, 0.65 and 0.91 μm (Figure 4b; Bishop and Murad, 2005). The $^6A_{1g}$ to ($^4A_{1g}$, ^4E_g)

465   transition was observed at 0.435 μm in the spectra of all three jarosite samples in this study. This

466   feature was observed at 0.436 μm in a jarosite spectrum presented in Crowley et al. (2003), at

467   0.435-0.437 μm in the jarosite spectra of Bishop and Murad (2005), and at 0.43-0.436 μm in

468   jarosite spectra obtained by Cloutis et al. (2006). The $^6A_{1g}$ to $^4T_{2g}$ transition is observed as a

469   shoulder in jarosite spectra and it is thus difficult to assign a wavelength for this absorption. It

470   was estimated here to be near 0.65 μm, which is in agreement with the 0.64-0.66 μm found

471   previously for jarosite (Bishop and Murad, 2005). The $^6A_{1g}$ to $^4T_{1g}$ transition was observed at

472   0.907 μm in the spectrum of our jarosite, at 0.915 μm in the spectrum of our hydronium jarosite,

473   and at 0.922 μm in the spectrum of our natrojarosite. This transition was identified at 0.924 μm

474   by Crowley et al. (2003), at 0.90-0.925 μm by Bishop and Murad (2005), and at 0.915-0.922 μm

475   by Cloutis et al. (2006). Slight variations in the shoulder near 0.65 and width of the 0.91-0.92 μm

476   band for the natrojarosite spectrum compared with the other jarosite type spectra could be due to

477   particle size, as the 45-125 μm size fraction was analyzed for the natrojarosite sample because

478   insufficient <45-μm material was available. This transition is observed as a doublet at 0.755 and

479   0.890 μm in the beaverite spectrum.

480   Additional NIR bands are observed near 1.47, 1.85, 2.22 (shoulder), 2.26, 2.41 (weak),

481   2.47 (weak), 2.51, and 2.62 μm due to overtones and combinations of the OH vibrations (Figure

482   4b; Bishop and Murad 2005). For the jarosite spectrum in our study these features are observed

483   at 1.469, 1.849, 2.264, 2.507, and 2.620 μm. For the hydronium jarosite spectrum they are found

484   at 1.470, 1.846, 2.268, 2.516, and 2.620 μm, for the natrojarosite spectrum they occur at 1.476,

485   1.847, 2.267, 2.516, and 2.620 μm and for the beaverite spectrum they are much weaker and

22

486   occur near 1.472, 1.865, 2.289, 2.516, and ~2.64 μm. The hydronium jarosite also exhibits an

487   H_2O stretching plus bending combination band at 1.94 μm. Weaker features are observed for the

488   jarosite and natrojarosite samples due to small amounts of adsorbed H_2O. The beaverite spectrum

489   includes a weak, broad H_2O combination band near 2.05 μm and a rounded H_2O/OH feature near

490   3 μm. The fundamental OH stretching band includes multiple overlapping vibrations and occurs

491   near 2.937 μm for jarosite, 2.953 μm for hydronium jarosite, and 2.946 μm for natrojarosite. A

492   number of small bands are also observed between 4.5-4.9 μm that are assigned to either an

493   overtone of the SO_4 ν_3 vibration or an overtone of the OH bending vibration (Bishop and Murad

494   2005).

495

496   **4.5. Infinite sheets of SO_4 tetrahedra and MX_6 octahedra**

497   **Goldichite:** The structure of goldichite (Rosenzweig and Gross 1954) is based on

498   corrugated sheets of [Fe(SO$_4$)$_2$ • 2 H_2O] clusters that link corner-shared octahedra and tetrahedra.

499   These sheets are connected by 9-coordinated K atoms and additional water molecules (i.e.,

500   hydrogen bond linkages) (Graeber and Rosenzweig 1971; Hawthorne 1985; Hawthorne et al.

501   2000) (Figure 5a). The spectrum of goldichite (Figure 5a) shows that constituent H_2O causes a

502   bending vibration (δH_2O) at ~1640 cm^{-1}; three ν_3 bands occur at 1258, 1169, and 1119 cm^{-1}, and

503   the ν_1 band is seen at 997 cm^{-1}. The ν_4 bands are at 689, 627, and 597 cm^{-1}; the ν_4 bands are at

504   476 and 428 cm^{-1}. Lattice modes occur at 359 cm^{-1} and in a band that is truncated at the edge of

505   the spectrum.

506   **Kornelite:** The structure of kornelite (Figure 5a) is based on corrugated sheets of

507   octahedral-tetrahedral layers of [Fe$_2$(H$_2$O)$_6$(SO$_4$)$_3$] attached to H_2O groups in the interlayer that

508   provide hydrogen bonding for linking the sheets (Robinson and Fang 1973; Hawthorne et al.

23

509   2000; Majzlan et al. 2005; Ackermann et al. 2009). The H_2O deformation band appears in the

510   emissivity spectrum (Figure 5a) at ~1665 cm^{-1} (albeit weakly) and a H_2O libration mode is seen

511   at 751 cm^{-1} according to a comparable assignment by Ling and Wang (2010). Four ν_3 features

512   are seen at 1206 (as a shoulder), 1160, 1121, and 1054 cm^{-1}. A ν_1 feature is apparent at 1020 cm^{-}

513   ^{1}. The ν_4 features occur at 627 and 593 cm^{-1} with a possible additional band at 650 cm^{-1} and the

514   ν_2 features occur at 492 and 448 cm^{-1}. Unfortunately, the spectrum does not extend to lower

515   wavenumbers below 400 cm^{-1} due to an operational error with the spectrometer.

516   **Rhomboclase:** The structure of rhomboclase is based on [$Fe(H_2O)_6(SO_4)_3$] groups with

517   additional interstitial (H_5O_2) groups that provide extensive hydrogen bonding (Hawthorne et al

518   2000). For rhomboclase, the bands in the emissivity spectrum (Figure 5a) are as follows: the H_2O

519   deformation mode (δH_2O) at ~1585 cm^{-1} (weak), and ν_3 bands at ~1210 (a shoulder), 1180, 1068

520   (a shoulder), and at 1043 cm^{-1}. The ν_1 band occurs at 1022 cm^{-1} with a δOH at 745 cm^{-1}. Two ν_4

521   bands are seen at 664 cm^{-1} and as a small band at ~627 cm^{-1}. A possible γOH feature is found at

522   593 cm^{-1}; a ν_2 band occurs at ~485 cm^{-1}; and a lattice mode occurs at 308 cm^{-1} along with a

523   lattice mode that is a truncated band so the actual position is not determined.

524   **Slavikite:** Slavikite is based on a sheet of corner-sharing octahedra and tetrahedra

525   (Hawthorne et al. 2000) of [$Fe_5(H_2O)_6(OH)_6(SO_4)_6$] that form into honeycomb-like structures

526   (Parafiniuketal et al. 2010) (Figure 5a). Holes in the open sheet are occupied by Na and H_2O

527   groups. The interlayer consists of {$Mg(H_2O)_6$} octahedra and disordered SO_4 tetrahedra that are

528   bound by hydrogen bonds. Although there are broad regions of reduced emission, this sample did

529   not produce a spectrum with clear, distinct features, even after pelletizing and deepening the

530   spectral features. Unfortunately, the overall sample size was so small that the pellet was really

531   just a thin (<<1 mm) chip about 5x7 mm^2 in area, so it could not produce a quality spectrum.

24

532   Nonetheless, the features that are discernible include: the broad H_2O deformation feature at

533   ~1612 cm^{-1}, ν_3 bands at 1199 and ~1084 cm^{-1}, a ν_1 band at ~1000 cm^{-1}, and ν_4 and ν_2 bands at

534   597 and 462 cm^{-1}, respectively. There is a clear lattice-mode band, but it is truncated so its

535   position is unknown.

536   **Yavapaiite:** The structure of yavapaiite consists of sheets of $[Fe(SO_4)_2]$ stacked in the *c*

537   axis direction and linked together by coplanar layers of 10-coordinated K atoms (Hawthorne

538   1985; Hawthorne et al. 2000). This configuration leads to perfect {001} cleavage (Graeber and

539   Rosenzweig 1971). For our work, we pressed a synthetic yavapaiite powder into a pellet to get a

540   spectrum devoid of volume scattering effects. As expected for a nominally anhydrous mineral,

541   our emissivity spectrum (Figure 5a) does not show any strong δH_2O, δOH, or γOH modes. The

542   ν_3 modes occur at 1254, ~1142 (as a shoulder), and 1024 cm^{-1}. No obvious ν_1 mode is seen at

543   lower wavenumbers than the ν_3 features, so it may be that the ν_1 mode lies within the ν_3 features

544   and is therefore unseen. This possibility is supported by the transmission spectrum of yavapaiite

545   shown in Forray et al. (2005) with four distinct features in the ~1000-1300 cm^{-1} range (likely

546   three ν_3 bands and a ν_1 feature). In our emissivity spectrum there also are distinct features at 676,

547   620, and 588 cm^{-1} that represent the ν_4 bands. The ν_2 bands are seen at 469, 444, and possibly

548   416 and 370 cm^{-1}. The 370 cm^{-1} band may be a metal-oxygen or lattice mode, plus there is

549   another longwave band that is truncated, but whose position may be at 255 cm^{-1}. Yavapaiite is

550   the anhydrous form of goldichite, and generally the yavapaiite bands (ν_3, ν_4, ν_2) appear at

551   smaller wavenumbers (i.e., lower frequencies) than the bands exhibited in the more-hydrous

552   goldichite. This trend is opposite that presented by Lane (2007) for the Ca-sulfate and Mg-sulfate

553   suites.

554

25

555   **VNIR Reflectance Data:** The crystal field bands vary widely for the sulfate minerals

556   with infinite sheets of SO_4 tetrahedra and MX_6 octahedra (Figure 5b) indicating a variety of Fe

557   sites for this mineral group. The goldichite spectrum exhibits only a very weak, broad Fe^{3+} $^6A_{1g}$

558   to $^4T_{1g}$ transition band centered near 0.89 μm that is consistent with a very low Fe content. The

559   kornelite spectrum has Fe^{3+} bands at 0.55 and 0.76 μm due to the $^6A_{1g}$ to $^4T_{2g}$ transition and $^6A_{1g}$

560   to $^4T_{1g}$ transition, respectively, which are similar to those of coquimbite, but otherwise unusual

561   for Fe sulfates or oxides. Thus, these bands are good spectral indicators for the presence of

562   kornelite or coquimbite. The rhomboclase spectrum includes a sharp Fe^{3+} $^6A_{1g}$ to ($^4A_{1g}$, ^4E_g)

563   transition at 0.430, a $^6A_{1g}$ to $^4T_{2g}$ transition at ~0.5 (shoulder), and $^6A_{1g}$ to $^4T_{1g}$ transition at 0.800

564   μm, similar to features observed by Crowley et al. (2003). The slavikite spectrum includes a

565   small sharp band at 0.43 μm and a broad band centered near 0.87 μm indicating a distribution of

566   the Fe^{3+} sites. The yavapaiite spectrum has Fe^{3+} bands at 0.425, ~0.52 (shoulder), and 0.735 μm.

567   The NIR spectrum of goldichite exhibits multiple doublet and triplet features akin to that

568   of sideronatrite, indicating splitting of the H_2O bands. The most prominent H_2O bands in the

569   goldichite spectrum occur at 1.426, 1.478, 1.768, 1.906, 2.169, 2.210, 2.320, 2.514 and 2.84 μm.

570   The kornelite spectrum contains weak H_2O bands at 1.16, 1.42, 1.92, 1.98 (broad), and 2.75 μm

571   and a completely saturated H_2O stretching band near 2.8-3.5 μm, whereas the rhomboclase

572   spectrum has a weak broad H_2O band near 1.25 μm followed by a drop in reflectance near 1.53

573   μm, a H_2O combination band near 2.0 μm, shoulders near 2.43 and 2.58 μm, and a weak, broad

574   H_2O stretching band near 2.8-2.95 μm. The NIR spectrum of slavikite somewhat resembles that

575   of gypsum with a triplet at 1.446, ~1.49, and 1.553 μm, a broad shoulder at 1.75 to 1.78 μm, a

576   strong combination band at 1.943 with a shoulder near 1.97 μm, a weak band at 2.12 μm, a

577   doublet at 2.224 and 2.266 μm, shoulders near 2.43 and 2.55 μm, and a strong, broad H_2O band

26

578   near 2.8-3.5 μm. Yavapaiite is anhydrous and its spectrum does not contain any H_2O vibrational

579   bands in the NIR region.

580   The yavapaiite spectrum exhibits multiple, strong SO_4 overtones and combinations from

581   4-5 μm. The dominant bands occur at 4.05, 4.12, 4.42, 4.52, 4.73, and a doublet at 4.88 and 4.92

582   μm. The goldichite spectrum includes multiple weak bands from ~4.2-4.9 due to SO_4 overtones

583   and combinations. The slavikite spectrum has a broad strong band centered near 4.5 μm and

584   another at 4.73 μm. The reflectance is very low for rhomboclase and kornelite spectra in the 3-5

585   μm region and sulfate bands are not observed for these minerals.

586

587   **4.6. Infinite frameworks of SO_4 tetrahedra and MX_6 octahedra**

588   **Szomolnokite:** The mineral szomolnokite is a monohydrated sulfate and it is the Fe-

589   endmember in a solid solution series with the Mg-endmember kieserite (Jambor et al. 2000).

590   Pure szomolnokite contains only Fe^{2+} cations and has a networked structure with $[Fe(SO_4)(H_2O)]$

591   chains that are cross-linked with other similar chains by corner sharing between octahedra and

592   tetrahedra of neighboring chains (Figure 6a). The szomolnokite hand sample is well crystalline

593   and provided strong features in the emissivity spectrum (Figure 6a). The szomolnokite spectrum

594   closely resembles a kieserite emissivity spectrum (Lane 2007); however, the szomolnokite

595   spectral features are shifted to longer wavelengths by 20-100 wavenumbers. The internal

596   vibrational bands due to the sulfate anion are distinct in the spectrum and consist of three v_3

597   bands at 1226, 1195, and 1149 cm^{-1}. The v_1 band appears as a small feature at 1018 cm^{-1}.

598   Features at 626, 606, and 554 cm^{-1} result from the v_4 vibrations. The feature at 361 cm^{-1} is a v_2

599   mode, but its assignment is uncertain. The truncated band at ~275 likely is due to a Fe-O

600   vibration.

27

601   In addition, there is a pronounced feature at 846 cm^{-1} that is uncommon in most sulfates

602   but is seen otherwise only in kieserite (at 919 cm^{-1}) (Lane 2007), among all the other sulfates

603   studied to date by the authors. This unusual feature is likely to appear also in a spectrum of

604   szmikite (a monohydrated Mn-sulfate of similar crystal structure), but to date a good sample has

605   not been obtained for analysis. This uncommon band likely is due to the unusual librational

606   mode (rocking) of the H_2O molecule seen in kieserite-group minerals but not in other hydrates in

607   which H_2O molecules form a similar coordination (Soptrajanov and Trpkovska 1993; Grodzicki

608   and Piszczek 1998). The presence of this band is a reliable indicator of monohydrated kieserite-

609   group sulfates (Lane 2007).

610   **Voltaite:** The structure of voltaite is more complex than that of many other Fe sulfates

611   and was determined by Mereiter (1972). The Fe^{2+}- and Fe^{3+}-containing structure consists of a

612   continuous framework of $[Fe^{3+}O_6]$ octahedra, $[Fe^{2+}_{5/6}Fe^{3+}_{1/6}O_4 (H_2O)_2]$ octahedra, and $[KO_{12}]$

613   polyhedra linked by (SO_4) tetrahedra. This structural arrangement allows disordered $[Al(H_2O)_6]$

614   octahedra to occupy the structure as well (Ertl et al. 2008) (Figure 6a). The voltaite emissivity

615   spectrum (Figure 6a) exhibits a H_2O deformation feature at ~1670 cm^{-1} but the broadness of the

616   feature makes the position uncertain. The ν_3 bands occur at 1171, ~1123 (shoulder), 1050, and

617   979 cm^{-1} (shoulder); the ν_1 feature occurs at 1004 cm^{-1}. The δOH bands are not sharp or strong

618   but possibly are at ~832 and ~735 cm^{-1}. The ν_4 bands are seen at 671 (subtle), 625, 584, and 520

619   cm^{-1}; ν_2 bands are seen at 469, 444, and possibly 416 cm^{-1}. Long-wave metal-oxygen/lattice

620   modes are seen at 370 cm^{-1} (possibly) and as a deep feature at 255 cm^{-1}, but the latter feature is

621   truncated and the spectral noise may mask the true position of this feature.

622

28

623   **VNIR Reflectance Data:** The crystal field bands are quite different for szomolnokite and

624   voltaite (Figure 6b). The szomolnokite spectrum includes a pair of Fe^{2+} bands something like that

625   observed for pyroxene (e.g., Cloutis and Gaffey 1991). The Fe^{2+} electronic excitation bands are

626   centered near 0.94 and 1.33 μm in the spectrum of our szomolnokite sample, and at 0.93 and

627   1.31 μm in a szomolnokite spectrum analyzed by Crowley et al. (2003). The spectrum of voltaite

628   has an Fe^{3+} electronic transition near 0.62 μm.

629   The voltaite spectrum exhibits H_2O features at 1.439, 1.719, 1.940, ~2.4, ~2.50, and 2.8-

630   3.5 μm, similar to other polyhydrated sulfates such as copiapite, römerite, and amarantite.

631   Szomolnokite is a monohydrated sulfate and its spectrum has very different H_2O bands, more

632   similar to those of kieserite (Bishop et al. 2009). The H_2O bands in the szomolnokite spectrum

633   occur at 1.520 μm for the H_2O stretching overtone, at 2.098 μm for the stretching plus bending

634   combination band, at 2.403 and 2.624 μm for additional H_2O bands, and a strong H_2O stretching

635   band occurs at ~2.9-3.3 μm.

636   The voltaite spectrum has an additional band at 4.0 μm and several weak bands from 4.5-

637   5 μm in the SO_4 overtone and combination band region, including absorptions at 4.82 and 4.96

638   μm. The szomolnokite spectrum includes multiple weak bands from 4.2-4.9 μm; the most

639   prominent bands are present at 4.34, 4.58, 4.70, 4.81, and 4.94 μm.

640

641   **5. Implications**

642   **5.1 Crystal structure**

643   Sulfate minerals are based on a repeated ordering of SO_4 tetrahedra polymerized with

644   MO_6 polyhedra (where *M* is a cation), and a majority of all sulfates (including Fe sulfates) are

645   hydrous (OH, H_2O). Of the 21 iron sulfates presented here, only one (yavapaiite) is nominally

29

646   anhydrous. Thermal emission spectra exhibit features related to the vibrational behavior and

647   interaction of the molecules within the sulfate mineral, and as such, their crystal structures

648   influence the character of their spectra. The figures in this paper are arranged by grouping

649   mineral spectra according to their molecular structure following the organization of Hawthorne

650   et al. (2000). This grouping should allow spectral similarities related to structure to stand out.

651   Cation complexation of the sulfate tetrahedron (that would not be deformed in it aqueous

652   state and would exhibit T_d site symmetry) causes distortions of the sulfate and changes the

653   symmetry to C_{3v}/ C_3 (monodentate, corner-sharing), C_{2v}/ C_2 (bidentate binuclear, edge-sharing),

654   or C_1/ C_s (bidentate binuclear, multidentate, corner-sharing, edge-sharing) (Myneni 2000). This

655   reduced symmetry causes band splitting, hence, the lower the symmetry of the sulfate, the more

656   additional features will be seen in the spectra (e.g., Adler and Kerr 1965; Myneni 2000).

657   Comparison among the sulfate emissivity figures shows that *all* the spectra are dominated

658   by deep bands related to the ν_3 vibrational modes that occur in the ~980 to 1270 cm^{-1} spectral

659   region and by a deep band(s) (beginning at $\leq$380 cm^{-1}), often truncated at the low-wavenumber

660   limit of our data related to M-O bonds or lattice vibrations (or H_2O libration). In addition to these

661   two deep band regions, the spectra of sulfates with sheets of $M_3(OH)_6(SO_4)_2$ (the

662   beaverite/jarosite group, Figure 4a) exhibit a third region of deep bands (~460-580 cm^{-1}) that are

663   approximately equivalent in depth to their ν_3 bands. The other structural groups do not exhibit

664   that behavior, but rather show weaker bands (ν_4, ν_2) in the spectral region between the ν_3 and the

665   long-wave (oft-truncated) bands.

666   Inspection of each iron sulfate structural group individually (i.e., each figure separately)

667   shows general spectral similarity within each iron sulfate mineral group. For example, in Figure

668   2a, the spectra exhibit a rather dominant, strong single ν_3 band (with other neighboring weaker

30

669   ν_3 bands). In Figure 3a, the spectra show a grouping of many ν_3 bands that are similarly deep. In

670   Figure 4a, the spectra show the ν_3 - ν_1 region in each spectrum as two divided groupings of

671   approximately similar-strength bands separated by an emissivity maximum (a flection position)

672   at ~ 1050-1075 cm^{-1} and, as mentioned above, this mineral group has the distinctive

673   characteristic of exhibiting a third deep grouping of bands (~460-580 cm^{-1}) that are similar in

674   depth to the ν_3 bands. And in Figure 5a, the ν_3 band grouping appears generally somewhat

675   asymmetrical with the deepest feature being on the low-wavenumber side. It is difficult to

676   generalize the spectra in Figure 6a beyond that they have a deep ν_3 band region and a deep long-

677   wave truncated band region; however, that general description would fit all of the sulfate group

678   spectra as mentioned above and is not unique to this structural group.

679   It is clear from this work that although Fe-sulfate minerals are dominated by the same

680   cation (Fe) and share similar structural units of SO_4 tetrahedra and MX_6 octahedra, their various

681   degrees of polymerization and unique crystal structure within their structure classes cause their

682   spectra to differ considerably. On a finer scale, however, the jarosite-series minerals (jarosite,

683   hydronium jarosite, natrojarosite) shown in Figure 4a show that in some cases, if the crystal

684   structure is the same but the cation is varied, the spectra are almost identical with only small

685   variation. Another good example of spectral similarity in sulfates when the crystal structure is

686   the same but the cation differs, lies with the mono-hydrated iron sulfate szomolnokite (Figure 6a)

687   and its Mg-bearing equivalent, kieserite ($MgSO_4 \cdot H_2O$). Lane (2007) showed that the spectra of

688   kieserite and szomolnokite are nearly identical, but the features of szomolnokite are shifted to

689   lower wavenumbers (see Figure 3 in Lane 2007). A final example, but in a different mineral

690   class, is the emissivity spectra of a suite of six-coordinated anhydrous carbonates (see Figure 2 in

31

691   Lane and Christensen 1997) for which the carbonate spectra all look almost identical, but the

692   fundamental bands are shifted due to the different cation in the crystal structure.

693   Historically, minerals have been grouped in various ways to relate and classify them,

694   such as by Nickel-Strunz groups (into ten primary groups; Strunz and Nickel 2001), Hey's

695   groups (into 32 more-focused groups, Clark 1993), and Dana groups (into 78 very specific

696   groups, Gaines et al. 1997). Investigation of the emissivity spectra shows that the shapes of the

697   Fe-sulfate mineral spectra are best predicted by the Dana class categorization, which is based on

698   structure type. For each mineral species, the Dana number consists of four different numbers

699   separated by periods. The first represents the Dana **class**, which is based on composition or

700   dominant structural elements. There are five classes that include sulfates:

701   Class 28 - Anhydrous Acid and Sulfates (e.g., yavapaiite, 28.03.04.01)

702   Class 29 - Hydrated Acid and Sulfates (e.g., rhomboclase, 29.01.01.01)

703   Class 30 - Anhydrous Sulfates Containing Hydroxyl or Halogen (e.g., jarosite,

704   30.02.05.01)

705   Class 31 - Hydrated Sulfates Containing Hydroxyl or Halogen (e.g., butlerite,

706   31.09.01.01)

707   Class 32 - Compound Sulfates (e.g., burkeite, 2.01.01.01).

708   The second number of the four represents the Dana **type**, which is based on the formula

709   and the number and ratios of cations. The third number represents the mineral **group** (e.g., the

710   alunite group) in which all species have the same structure, and the last number is assigned to the

711   individual **species**. This work has demonstrated that samples in the same group generally have

712   very similar spectra, and samples in the same Dana type are often quite similar as well. For

713   example, kieserite (29.6.2.1) and szomolnokite (29.6.2.2.) are both members of the kieserite

32

714   group (29.6.2) along with gunningite, dwornikite, poltevinite, szmikite, and cobaltkieserite. It is

715   not necessary to acquire data from all the species in this group to know that their spectra will be

716   similar – although it should be noted that even at the species level, the spectra within a group are

717   not exactly the same and shifted. Rather, they are very similar in spectral shape and shifted, but

718   the fundamental features do not translate exactly. For some spectra, the bands move in opposite

719   directions or at different rates, or some bands merge or vary in other subtle ways, but the overall

720   spectral shape remains distinct. Nonetheless, at this level of classification, the spectra are similar

721   enough that the expert spectroscopist should be able to identify the mineral group and series, and

722   likely the exact mineral species, if that species exists in the spectral database.

723   The VNIR reflectance spectra of the Fe sulfates are highly dependent on the environment

724   of the Fe in the crystal structure and the degree of hydration. The most common crystal field

725   band occurs near 0.78-0.93 µm for Fe^{3+} in sulfates. Additional electronic transitions occur in

726   some minerals as a sharp and usually weak band at 0.43 µm and a shoulder near 0.5-0.65 µm.

727   The spectra of kornelite and coquimbite are unique in that they have two strong crystal field

728   bands near 0.55-0.56 and 0.76-0.78 µm. Fe^{2+} in sulfate spectra exhibit crystal field bands near

729   0.94-1.2 µm and occasionally a second crystal field band at longer wavelengths as in the case of

730   szomolnokite. The H_2O bands are present as smooth, broad bands near 1.45, 1.95, 2.5 and 3 µm

731   in several Fe sulfates such as amarantite, copiapite, and rozenite. Other Fe-sulfate spectra exhibit

732   H_2O bands that are split into doublets or triplets such as goldichite, slavikite and sideronatrite. Fe

733   sulfates containing OH in their structure such as jarosite and butlerite have spectral features due

734   to OH near 1.42-1.47, 2.2-2.3, and 2.7-2.8 µm. Anhydrous Fe sulfates like yavapaiite do not

735   exhibit spectral features in the range 1-3 µm.

736

33

737   **5.2 Mars Geochemistry**

738   Many iron sulfate minerals exist both on Earth, often in acid mine drainage (AMD) sites,

739   and on Mars. They form via oxidation of sulfides that can precipitate secondary hydrous oxides,

740   hydroxysulfates, and divalent-metal (M^{2+}) sulfates (e.g., commonly melanterite), and generally

741   lead to the generation of acidic solutions (e.g., Jambor et al. 2000; Jerz and Rimstidt 2005; King

742   and McSween 2005). Although the M^{2+} in sulfates can be Fe, Mn, Co, Ni, Mg, Cu, or Zn,

743   precipitation of Fe-sulfates (followed by Mg-) are dominant in AMD environments (Jambor et al.

744   2000). Further oxidation, dehydration, and/or neutralization will alter the Fe^{2+} sulfates to a wide

745   suite of other Fe^{3+}/Fe^{2+} or exclusively Fe^{3+} sulfates. The presence of Fe sulfates generally implies

746   acidic conditions, so their continued and mineral-specific identification on Mars (e.g.,

747   Klingelhöfer et al. 2004; Wang et al. 2006; Morris et al. 2006; Johnson et al. 2007; Lane et al.

748   2008; Milliken et al. 2008; Bishop et al. 2009) can help aid in the interpretation of the chemical

749   environments and geologic settings in the past and on present-day Mars (e.g., Fe^{2+} sulfates are

750   generally more water soluble than Fe^{3+} sulfates and would imply a water-limited environment;

751   Fe^{3+} sulfates form over a range of hydration levels but are an indication of more oxidation along

752   with low pH, etc.). Each specific Fe-sulfate mineral identification constrains the bulk chemistry

753   and lends more information about the specific formational environment. For example,

754   rhomboclase prefers lower pH (<0) and jarosite prefers a higher pH (2-4) than other Fe-sulfates

755   (e.g., ferricopiapite (pH <2); Majzlan et al. 2006), and yavapaiite is obtainable through thermal

756   decomposition (dehydration) of jarosite (Forray et al. 2005). Dehydration of coquimbite can

757   produce kornelite (Robinson and Fang 1973) that can further dehydrate to pentahydrated Fe^{3+}

758   sulfate (Kong et al. 2011) or rhomboclase (Lane et al. 2008). Rhomboclase also has been seen to

759   hydrate to form kornelite (King, unpublished data) suggesting that the reaction is reversible.

34

760   Dehydration of melanterite will produce rozenite, which is common on Earth (Kubisz 1960;

761   Kossenberg and Cook 1961; Jambor et al. 2000) and over time in a dry (or higher temperature)

762   environment rozenite (or melanterite) can further dehydrate to szomolnokite (Bolshakov and

763   Ptushko 1971); sometimes the intermediate rozenite is not observed (e.g., Hyde et al. 2011).

764   Long-term paragenesis of Fe^{3+} sulfates in oxidative environments will produce schwertmannite

765   (or jarosite-family minerals if other cations are available) prior to forming Fe oxyhydroxides

766   (Jambor et al. 2000; King and McSween 2005); and there are numerous other examples of how

767   specific formational environments relate to the bulk chemistry and *visa versa*.

768   Oxidation of Fe^{2+} in acid solutions occurs abiologically but also can occur biologically

769   through the presence of oxidizing bacteria such as *Thiobacillus ferrooxidans* (e.g., Lazaroff et al.

770   1982), and Fe^{3+} sulfates depress the freezing point of brines (Chevrier and Altheide, 2008),

771   hence identification of Fe^{3+} sulfates on Mars may be important for selecting future regions of

772   study intended for the study of life on Mars. Finally, Fe sulfates are capable of hosting a

773   significant amount of H_2O in their crystal structures (Table 1) and may be part of the phases in

774   the martian bulk soil that link mineralogy to the amount of water-equivalent hydrogen (WEH)

775   identified by the orbiting Mars Odyssey Gamma Ray Spectrometer (Boynton et al. 2002;

776   Feldman et al. 2002, 2004; Karunatillake et al. 2012, 2013).

777   Not only do specific Fe-sulfate minerals form in specific and predictable chemical

778   environments, but each Fe-sulfate mineral exhibits a unique thermal emissivity and visible/near-

779   infrared spectrum that acts as a spectral fingerprint for that mineral. The Fe-sulfate spectra

780   presented in this work will enable scientists to identify these sulfates on Mars and determine

781   what the chemical environment was on Mars during their formation.

782

35

795

796   **References**

797   Ackermann, S., Lazic, B., Armbruster, T., Doyle, S., Grevel, K.-D., and Majzlan, J. (2009)

798   Thermodynamic and crystallographic properties kornelite [$Fe_2(SO_4)_3 \bullet \sim7.75\ H_2O$] and

799   paracoquimbite [$Fe_2(SO_4)_3 \bullet 9\ H_2O$]. American Mineralogist, 94, 1620-1628.

800   Adler, H. H. and P. F. Kerr, Variations in infrared spectra, molecular symmetry and site

801   symmetry of sulfate minerals, American Mineralogist, 50, 132-147, 1965.

802   Anderson, J. L., R. C. Peterson, and I. P. Swainson (2007) The atomic structure and hydrogen

803   bonding of deuterated melanterite, $FeSO_4 \cdot 7D_2O$. The Canadian Mineralogist, 45, 457-

804   469.

36

805   Apopei, A. I., Damian, G, and Buzgar, N. (2012) A preliminary Raman and FT-IR spectroscopic

806   study of secondary hydrated sulfate minerals from the Hondol open pit. Romanian

807   Journal of Mineral Deposits, 85 (2), 1-6.

808   Aronson, J. R. and Emslie, A. G. (1973) Spectral reflectance and emittance of particulate

809   materials, 2, Application and results. Applied Optics, 12, 2573-2584.

810   ___, ___, and McLinden, H. G. (1966) Infrared spectra from particulate surfaces. Science, 152,

811   345-346.

812   Arvidson, R., Poulet, F., Bibring, J.-P., Wolff, M. Gendrin, A., Morris, R. V., Freeman, J. J.,

813   Langevin, Y., Mangold, N., and Bellucci, G. (2005) Spectral reflectance and morphologic

814   correlations in eastern Terra Meridiani, Mars. Science, 307, 1591-1594.

815   Athena Mineralogy URL, http://athena.unige.ch/athena/mineral/minppcl6.html

816   Baldridge, A., P. R. Christensen, and M. D. Lane (2014) Thermal emission characterization of

817   magnesium sulfates. American Mineralogist, this issue.

818   Basciano, L.C., and Peterson, R.C. (2007) Jarosite - hydronium jarosite solid solution series with

819   full iron occupancy: Mineralogy and crystal chemistry. American Mineralogist, 92, 1464-

820   1473.

821   Baur, W. H. (1962) Zur kristallchemie der salzhydrate. Die kristallstrukturen von $MgSO_4 \cdot 4H_2O$

822   (leonhardtit) und $FeSO_4 \cdot 4H_2O$ (rozenit). Acta Crystallographica, 15, 815-826.

823   Bigham J. M., Carlson L., and Murad E. (1994) Schwertmannite, a new iron oxyhydroxysulphate

824   from Pyhäsalmi, Finland, and other localities. Mineralogical Magazine, 58, 641-648.

37

825   Binder, A. B., Arvidson, R. E., Guinness, E. A., Jones, K. L., Morris, E. C., Mutch, T. A., Pieri,

826   D. C., and Sagan, C. (1977) The geology of the Viking Lander 1 site. Journal of

827   Geophysical Research, 82, 4439-4451.

828   Bish, D.L., Carey, J. W., Vaniman, D.T., and Chipera, S. J. (2003) Stability of hydrous minerals

829   on the martian surface. Icarus, 164, 96-103.

830   Bishop J. L. and Murad E. (1996) Schwertmannite on Mars? Spectroscopic analyses of

831   schwertmannite, its relationship to other ferric minerals, and its possible presence in the

832   surface material on Mars. In M. D. Dyar, C. McCammon, and M. W. Schaefer, Eds.,

833   Mineral Spectroscopy: A tribute to Roger G. Burns, Special Publication Number 5, p.

834   337-358. The Geochemical Society. Houston, TX.

835   ___ and ___ (2005) The visible and infrared spectral properties of jarosite and alunite. American

836   Mineralogist, 90(7), 1100-1107.

837   ___, Dyar, M. D., Lane, M. D., and Bandfield, J. (2005) Spectral identification of hydrated

838   sulfates on Mars and comparison with acidic environments on Earth. International Journal

839   of Astrobiology, 3 (4), 275-285.

840   ___, Parente, M., Weitz, C. M., Noe Dobrea, E. Z., Roach, L. H., Murchie, S. L., McGuire, P. C.,

841   McKeown, N. K., Milliken, R., and J. F. Mustard (2009) Mineralogy of Juventae Chasma:

842   Sulfates in the light-toned mounds, mafic minerals in the bedrock, and hydrated silica and

843   hydroxylated ferric sulfate on the plateau. Journal of Geophysical Research, 114, E00D09,

844   doi: 10.1029/2009JE003352.

845   Bolshakov, A. P. and Ptushko, L. I. (1971) Alteration products of melanterite from the Nikitov

846   mercury ore deposits. International Geology Review, 13, 849-854.

38

847   Boynton, W. V., Feldman, W. C., Squyres, S. W., Prettyman, T. H., Brückner, J., Evans, L. G.,

848   Reedy, R. C., Starr, R., Arnold, J. R., Drake, D. M., Englert, P. A. J., Metzger, A. E.,

849   Mitrofanov, I., Trombka, J. I., d'Uston, C., Wänke, H., Gasnault, O., Hamara, D. K.,

850   Janes, D. M., Marcialis, Maurice, S., Mikheeva, I., Taylor, G. J., Tokar, R., and

851   Shinohara, C. (2002) Distribution of hydrogen in the near surface of Mars: Evidence for

852   subsurface ice deposits. Science, 297, 81-85.

853   Breidenstein, B., Schlüter, J., and G. Gebhard (1992) On beaverite: New occurrence, chemical

854   data, and crystal structure. Neues Jahrbuch für Mineralogie, Monatshefte, 213-220.

855   Brown, R. G. and Ross, S. D. (1970) Forbidden transitions in the infra-red spectra of tetrahedral

856   anions – VI. Tutton's salts and other double sulphates and selenates. Spectrochimica Acta,

857   26A, 945-953.

858   Burns, R. G. (1987) Ferric sulfates on Mars. Journal Geophysical Research 92, 570-574.

859   ___ (1993) Rates and mechanisms of chemical weathering of ferromagnesian silicate minerals on

860   Mars. Geochimica et Cosmochimica Acta, 57, 4555-4574.

861   Chevrier, V. F. and Altheide, T. S. (2008) Low temperature aqueous ferric sulfate solutions on the

862   surface of Mars. Geophysical Research Letters, 35, L22101.

863   Chio, C. H., Sharma, S. K., and Muenow, D. W. (2004) Micro-Raman studies of gypsum in the

864   temperature range between 9K and 373K. American Mineralogist, 89, 390-395.

865   ___, ___, and ___ (2007) The hydrates and deuterates of ferrous sulfate ($FeSO_4$): A Raman

866   spectroscopic study. Journal of Raman Spectroscopy, 38, 87-99.

867   Christensen, P. R. and Harrison, S. T. (1993) Thermal infrared emission spectroscopy of natural

868   surfaces: Application to desert varnish coatings on rocks. Journal of Geophysical

869   Research, 98, 19819-19834.

870   Clark, A. M. (1993) Hey's Mineral Index, Mineral Species, Varieties and Synonyms, 3rd edition,

871   Chapman and Hall, London, 852 pp.

872   Clark, R. N. (1999) Chapter 1: Spectroscopy of Rocks and Minerals, and Principles of

873   Spectroscopy. In A. N. Rencz, Ed. Manual of Remote Sensing, Volume 3, Remote

874   Sensing for the Earth Sciences, John Wiley and Sons, New York, p. 3-58.

875   Cloutis E.A. and Gaffey M.J. (1991) Pyroxene spectroscopy revisited: Spectral-compositional

876   correlations and relationships to geothermometry. Journal of Geophysical Research, 96,

877   22809-22826.

878   ___, Hawthorne, F. C., Mertzman, S. A., Krenn, K., Craig, M. A., Marcino, D., Methot, M.,

879   Strong, J., Mustard, J. F., Blaney, D. L., Bell III, J. F., and Vilas, F. (2006) Detection and

880   discrimination of sulfate minerals using reflectance spectroscopy. Icarus, 184, 121-157.

881   Crowley J.K., Williams D.E., Hammarstrom J.M., Piatak N., Chou I.-M., and Mars J.C. (2003)

882   Spectral reflectance properties (0.4-2.5 μm) of secondary Fe-oxide, Fe-hydroxide, and

883   Fe-sulphate-hydrate minerals associated with sulphide-bearing mine wastes.

884   Geochemistry: Exploration, Environment, Analysis, 3, 219-228.

885   Della Ventura, G., Ventruti, G., Bellatreccia, F., Scordari, F., and Guidi, M. C. (2013) FTIR

886   transmission spectroscopy of sideronatrite, a sodium-iron hydrous sulfate. Mineralogical

887   Magazine, 77 (4), 499-507.

888   Deer, W. A., Howie, R. A., and Zussman, J. (1997) *Rock-Forming Minerals*, 2nd ed., Geological

889   Society of London.

890   Dyar, M. D., Breves, E. A., Jawin, E., Marchand, G., Nelms, M., O'Connor, V., Peel, S.,

891   Rothstein, Y., Sklute, E. C., Lane, M. D., Bishop, J. L., and Mertzman, S. A. (2014)

40

892   Mössbauer parameters of iron in sulfate minerals. American Mineralogist, v. 98, no. 11-

893   12, pp. 1943-1965, doi:10.2138/am.2013.4604.

894   Ertl, A., Dyar, M. D., Hughes, J. M., Brandstätter, F., Gunter, M. E., Prem, M., Peterson, R. C.

895   (2008) Pertlikite, a new tetragonal Mg-rich member of the voltaite group from Madeni

896   Zakh, Iran. The Canadian Mineralogist, 46, 661-669.

897   Fafani, L., Nunzi, A., and Zanazzi, P. F. (1970) The crystal structure of roemerite. American

898   Mineralogist, 55, 78-89.

899   ___, ___, and ___ (1971) The crystal structure of butlerite. American Mineralogist, 56, 751-757.

900   Fang, J.H., and Robinson, P.D. (1970) Crystal structures and mineral chemistry of hydrated

901   ferric sulfates. I. The crystal structure of coquimbite. American Mineralogist, 55, 1534-

902   1540.

903   Feldman, W. C., Boynton, W. V., Tokar, R. L., Prettyman, T. H., Gasnault, O., Squyres, S. W.,

904   Elphic, R. C., Lawrence, D. J., Lawson, S. L., Maurice, S., McKinney, G. W., Moore, K.

905   R., and Reedy, R. C. (2002) Global distribution of neutrons from Mars: Results from

906   Mars Odyssey. Science, 297, 75-78.

907   Feldman, W. C., Mellon, M. T., Maurice, S., Prettyman, T. H., Carey, J. W., Vaniman, D. T.,

908   Bish, D. L., Fialips, C. I., Chipera, S. J., Kargel, J. S., Elphic, R. C., Funsten, H. O.,

909   Lawrence, D. J., and Tokar, R. L. (2004) Hydrated states of $MgSO_4$ at equatorial latitudes

910   on Mars. Geophysical Research Letters, 31, doi:10.1029/2004GL020181.

911   ___, Prettyman, T. H., Maurice, S., Plaut, J. J., Bish, D. L., Vaniman, D. T., Mellon, M. T.,

912   Metzger, A. E., Squyres, S. W., Karunatillake, S., Boynton, W. V., Elphic, R. C.,

913   Funsten, H. O., Lawrence, D. J., and Tokar, R. L. (2004) Global distribution of near-

914   surface hydrogen on Mars. Journal of Geophysical Research, 109, E09006,

41

915   doi:10.1029/2003JE002160.

916   Gaines, R. V., Skinner, C. W., Foord, E. E., Mason, B., and Rozenzweig, A. (1997) Dana's new

917   mineralogy – The system of mineralogy of James Dwight Dana and Edward Salisbury

918   Dana, 8th edition, entirely rewritten and greatly enlarged, John Wiley & Sons, New York,

919   1819 pp.

920   Gendrin, A., Mangold, N., Bibring, J.-P., Langevin, Y., Gondet, B., Poulet, F., Bonello, G.,

921   Quantin, C., Mustard, J., Arvidson, R., LeMouelic, S. (2005) Sulfates in marian layered

922   terrains: The OMEGA/Mars Express view. Science, 307, 1587-1591.

923   Graeber, E. J. and A. Rosenzweig (1971) The crystal structures of yavapaiite, $KFe(SO_4)_2$, and

924   goldichite $KFe(SO_4)_2 \cdot H_2O$. American Mineralogist, 56, 1917-1933.

925   Griffen, D. T. and Ribbe, P. H. (1979) Distortions in the tetrahedral oxyanions of crystalline

926   substances. Neues Jahrbuch für Mineralogie, Abhandlungen, 137, 54-73.

927   Grodzicki, A., and Piszczek, P. (1998) A new interpretation of abnormal shift of water

928   molecules' bending vibration frequencies in kieserite family monohydrates. Journal of

929   Molecular Structure, 443, 141-147.

930   Hapke, B. (1993) Theory of Reflectance and Emittance Spectroscopy, 455 pp., Cambridge

931   University Press, New York.

932   Hawthorne, F. C. (1985) Towards a structural classification of minerals: The $^{VI}M^{IV}T_2\Phi_n$

933   minerals. American Mineralogist, 70, 455-473.

934   ___, Krivovichev, S. V., and Burns, P. C. (2000) The crystal chemistry of sulfate minerals. In C.

935   N. Alpers, J. L. Jambor, and D. K. Nordstrom, Eds. Sulfate Minerals: Crystallography,

42

936   Geochemistry, and Environmental Significance, 40, 1-112. Reviews in Mineralogy and

937   Geochemistry, Mineralogical Society of America, Washington, D. C.

938   Herzberg, G. (1945) Infrared and Raman Spectra of Polyatomic Molecules, Van Nostrand, NY.

939   Hezel, A. and Ross, S. D. (1966) Forbidden transitions in the infra-red spectra of tetrahedral

940   anions—III. Spectra-structure correlations in perchlorates, sulphates and phosphates of

941   the formula MXO_4. Spectrochimica Acta, 22, 1949-1961.

942   Hug, S. J. (1997) In situ Fourier transform infrared measurements of sulfate adsorbed on

943   hematite in aqueous solutions. Journal of Colloid and Interface Science, 188, 415-422.

944   Hunt, G. R. and Logan, L. M. (1972) Variation of single particle mid-infrared emission spectrum

945   with particle size. Applied Optics, 11, 142-147.

946   ___ and Vincent, R. K. (1968) The behavior of spectral features in the infrared emission from

947   particulate surfaces of various grain sizes. Journal of Geophysical Research, 73, 6039-

948   6046.

949   ___, Salisbury J.W., and Lenhoff C.J. (1971) Visible and near-infrared spectra of minerals and

950   rocks: IV. Sulphides and sulphates. Modern Geology, 3, 1-14.

951   Hyde, B. C., King, P. L, Dyar, M. D., Spilde, M. N., and Ali, A.-M. S. (2011) Methods to

952   analyze metastable and microparticulate hydrated and hydrous iron sulfate minerals.

953   American Mineralogist, 96, 1856-1869.

954   Jakosky, B. M. and Christensen, P. R. (1986) Global duricrust on Mars – Analysis of remote-

955   sensing data. Journal of Geophysical Research, 91, 3547-3559.

956   Jambor, J. L., Nordstrom, D. K., and Alpers, C. N. (2000) Metal-sulfate salts from sulfide

957   mineral oxidation. In C. N. Alpers, J. L. Jambor, and D. K. Nordstrom, Eds. Sulfate

43

958   Minerals: Crystallography, Geochemistry, and Environmental Significance, 40, 303-350.

959   Reviews in Mineralogy and Geochemistry, Mineralogical Society of America,

960   Washington, D. C.

961   Jerz, J. K. and Rimstidt, J. D. (2003) Efflorescent iron sulfate minerals: Paragenesis, relative

962   stability, and environmental impact. American Mineralogist, 88, 1919-1932.

963   Johnson, J. R., Bell III, J. F., Cloutis, E., Staid, M. S, Farrand, W. H., McCoy, T., Rice, M.,

964   Wang, A., and Yen, A. (2007) Mineralogic constraints on sulfur-rich soils from Pancam

965   spectra at Gusev crater, Mars. Geophysical Research Letters, 34,

966   doi:10.1029/2007/GL029894.

967   Karunatillake, S., Gasnault, O., McLennan, S. M., Rogers, A. D., Wray, J. J., Squyres, S. W.,

968   Boynton, W. V. (2012) The hydration state of sulfates on Mars. In *Lunar and Planet. Sci.*

969   *XLIII*, Abstract #2940, Lunar and Planetary Institute, Houston (CD-ROM).

970   Karunatillake, S., Wray, J. J., Gasnault, O., McLennan, S. M., Rogers, A. D., Squyres, S. W., and

971   Boynton, W. V. (2013) Regional prevalence of Fe-sulfates on Mars. In *The Present-day*

972   *Habitability of Mars Conference*, Institute for Planets and Exoplanets, University of

973   California at Los Angeles.

974   King, P. L. and McSween Jr., H. Y. (2005) Effects of H_2O, pH, and oxidation state on the

975   stability of Fe minerals on Mars. Journal of Geophysical Research, 110, E12S10,

976   doi:10.1029/2005JE002482.

977   Klingelhofer, G., Morris, R. V., Bernhardt, B., Schröder, C., Rodionov, D. S., de Souza Jr., P. A.,

978   Yen, A., Gellert, R., Evlanov, E. N., Zubkov, B., Foh, J., Bonnes, U., Kankeleit, E.,

979   Gütlich, P., Ming, D. W., Renz, F., Wdowiak, T., Squyres, S. W., and Arvidson, R. E.

44

980   (2004) Jarosite and hematite at Meridianin Planum from Opportunity's Mössbauer

981   spectrometer. Science, 306, 1740-1745.

982   Kong, W. G., Wang, A., and Chou, I.-M. (2011) Experimental determination of the phase

983   boundary between kornalite and pentahydrated ferric sulfate at 0.1 MPa. Chemical

984   Geology, 284, 333-338.

985   Kossenberg, M. and Cook, A. C. (1961) Weathering of sulphide minerals in coal; production of

986   ferrous sulphate heptahydrate. Mineral Magazine, 32, 829-830.

987   Kubisz, J. (1960) Rozenite, $FeSO_4 \cdot 4 H_2O$, a new mineral. Bulletin of the Polish Academy of

988   Sciences, Ser. Sci. Geol. Geogr., 8, 107-113.

989   Lane, M. D. (1999) Midinfrared optical constants of calcite and their relationship to particle size

990   effects in thermal emission spectra of granular calcite. Journal of Geophysical Research,

991   104, 14099-14108.

992   ___ (2007) Midinfrared emission spectroscopy of sulfate and sulfate-bearing minerals. American

993   Mineralogist, 92, 1-18.

994   ___ and Christensen, P. R. (1997) Thermal infrared emission spectroscopy of anhydrous

995   carbonates. Journal of Geophysical Research, 102, 25581-25592.

996   ___, Bishop, J. L., Dyar, M. D. King, P. L., Parente, M., and Hyde, B. C. (2008) Mineralogy of

997   the Paso Robles soils on Mars. Amer. Mineral., 93, 728-739.

998   ___, Dyar, M. D., and Bishop, J. L. (2004) Evidence for hydrous iron sulfate in the Martian soil.

999   Geophysical Research Letters, 31, L19702, doi:10.1029/2004GL021231.

45

1000 Lazaroff, N., Sigal, W., and Wasserman, A. (1982) Iron oxidation and precipitation of ferric

1001   hydroxysulfates by resting *Thiobacillus ferrooxidans* cells. Applied and Environmental

1002   Microbiology, 43(4), 924-938.

1003 Libowitzky, E. (1999) Correlation of O-H stretching frequencies and O-H···O-H bond lengths in

1004   minerals. Monatshefte für Chemie, 130, 1047-1059.

1005 Ling, Z. C. and Wang, A. (2010) A systematic spectroscopic study of eight hydrous ferric

1006   sulfates relevant to Mars. Icarus, 209, 422-433.

1007 Lyon, R. J. P. (1964) Evaluation of infrared spectrophotometry for compositional analysis of

1008   lunar and planetary soils, II, Rough and powdered surfaces. NASA Conference Report

1009   CR-100.

1010 Majzlan, J. and Michallik, R. (2007) The crystal structures, solid solutions and infrared spectra

1011   of copiapite-group minerals. Mineralogical Magazine, 71 (5), 553-569.

1012 ___, Alpers, C. N., Bender Koch, C., McCleskey, R. B., Myneni, S. C. B., and Neil, J. M. (2011)

1013   Vibrational, X-ray absorption, and Mössbauer spectra of sulfate minerals from the

1014   weathered massive sulfide deposit at Iron Mountain, California. Chemical Geology, 284,

1015   296-305.

1016 ___, Botez, C., and Stephens, P. W. (2005) The crystal structures of synthetic $Fe_2(SO_4)_3(H_2O_5)$

1017   and the type specimen of lausenite. American Mineralogist, 90, 411-416.

1018 ___, Navrotsky, A., McCleskey, R. B., and Alpers, C. N. (2006) Thermodynamic properties and

1019   crystal   structure   refinement   of   ferricopiapite,   coquimbite,   rhomboclase,   and

1020 $Fe_2(SO_4)_3(H_2O_5)$. European Journal of Mineralogy, 18, 175-186.

46

1021   Makreski, P., Jovanovski, G., Dimitrovska, S. (2005) Minerals from Macedonia: XIV.

1022   Identification of some sulfate minerals by vibrational (infrared and Raman) spectroscopy.

1023   Vibrational Spectroscopy, 39, Issue 2, 229-239.

1024   Mereiter, K. (1972) Die Kristallstruktur des Voltaits, $K_2Fe^{2+}_5Fe^{3+}_3O_4Al[SO_4]_{12}$ • 18 H_2O.

1025   Tschermaks Mineral. Petrogr. Mitt., 18, 185-202.

1026   ___ (1974) Die Kristallstruktur von Rhomboklas, $H_5O_2^+${$Fe[SO_4]_2·2H_2O$}. Tschermaks

1027   Mineralogische und Petrographische Mitteilungen, 21, 216-232.

1028   Millikin, R. E., Swayze, G. A., Arvidson, R. E., Bishop, J. L., Clark, R. N., Ehlmann, B. L.,

1029   Green, R. O., Grotzinger, J. P., Morris, R. V., Murchie, S. L., Mustard, J. F., and Weitz, C.

1030   Opaline silica in young deposits on Mars. Geology, 36, 847-850.

1031   Moenke, H. (1962) Mineralspektren I: Die Ultrarotabsorption der häufigsten und wirtschaftlich

1032   wichtigsten Halogenid-, Oxyd-, Hydroxyd-, Carbonat-, Nitrat-, Borat-, Sulfat-, Chromat-,

1033   Wolframat-, Molybdat-, Phosphat-, Arsenat-, Vanadat- und Silikatmineralien im

1034   Spektralbereich 400-4000 cm^{-1}. Akademie Verlag, Berlin.

1035   Moersch, J. E. (1992) Modeling Particle Size Effects on the Emissivity Spectra of Minerals in

1036   the Thermal Infrared, M. S. thesis, Arizona State Univ., Tempe, AZ.

1037   ___ and Christensen, P. R. (1995) Thermal emission from particulate surfaces: A comparison of

1038   scattering models with measured spectra. Journal of Geophysical Research, 100, 7465-

1039   7477.

1040   Morris, R. V., Klingelhofer, G., Schröder, C., Rodionov, D. S., Yen, A., Ming, D. W., de Souza

1041   Jr., P. A., Wdowiak, T., Fleischer, I., Gellert, R., Bernhardt, B., Bonnes, U., Cohen, B.

1042   A., Evlanov, E. N., Foh, J., Gütlich, P., Kankeleit, E., McCoy, T., Mittlefehldt, D. W.,

47

1043 Renz, F., Schmidt, M. E., Zubkov, B., Squyres, S. W., and Arvidson, R. E. (2006)

1044 Mössbauer mineralogy of rock, soil, and dust at Meridiani Planum, Mars: Opportunity's

1045 journey across sulfate-rich outcrop, basaltic sand and dust, and hematite lag deposits.

1046 Journal of Geophysical Research, 111, doi: 10.1029/2006JE002791.

1047 Murchie, S., Roach, L., Seelos, F., Milliken, R., Mustard, J., Arvidson, R., Wiseman, S.,

1048 Lichtenberg, K., Andrews-Hanna, J., Bishop, J., Bibring, J.-P., Parente, M., and Morris,

1049 R. (2009) Evidence for the origin of layered deposits in Candor Chasma, Mars, from

1050 mineral composition and hydrologic modeling. Journal of Geophysical Research, 114,

1051 E00D05, doi: 10.1029/2009JE003343.

1052 Mustard, J. F. and Hays, J. E. (1997) Effects of hyperfine particles on reflectance spectra from

1053 0.3 to 25 mm. Icarus , 125, 145-163.

1054 Mutch, T. A., Arvidson, R. E., Binder, A. B., Guinness, E. A., Morris, E. C. (1977) The geology

1055 of the Viking Lander 2 site. Journal of Geophysical Research, 82, 4452-4467.

1056 Myneni, S. (2000) X-ray and vibrational spectroscopy of sulfate in earth materials. In C. N.

1057 Alpers, J. L. Jambor, and D. K. Nordstrom, Eds. Sulfate Minerals: Crystallography,

1058 Geochemistry, and Environmental Significance, 40, 113-172. Reviews in Mineralogy and

1059 Geochemistry, Mineralogical Society of America, Washington, D. C.

1060 Nakamoto, K. (1986) Infrared and Raman Spectra of Inorganic and Coordination Compounds,

1061 Wiley & Sons, NY.

1062 Omori, K. and Kerr, P. F. (1963) Infrared studies of saline sulfate minerals. Geological Society

1063 of America Bulletin, 74, 709-734.

48

1064   Parafiniuk, J., Dobrzycki, L., and Wozniak, K. (2010) Slavikite – revision of chemical

1065   composition and crystal structure. American Mineralogist, 95, 11-18.

1066   Peterson, R.C. (2003) The relationship between Cu content and distortion in the atomic structure

1067   of melanterite from the Richmond mine, Iron Mountain, California. The Canadian

1068   Mineralogist, 41, 937-949.

1069   Powers, D. A., Rossman, G. R., Schugar, H. J., and Gray, H. B. (1975) Magnetic behavior and

1070   infrared spectra of jarosite, basic iron sulfate, and their chromate analogs. Journal of

1071   Solid State Chemistry, 13, 1-13.

1072   Roach, L. H., Mustard, J. F., Murchie, S. L., Bibring, J.-P., Forget, F., Lewis, K. W., Aharonson,

1073   O., Vincendon, M., and Bishop, J. L. (2009) Testing evidence of recent hydration state

1074   change in sulfates on Mars. Journal of Geophysical Research, 114, E00D02, doi:

1075   10.1029/2008JE003245.

1076   Robinson, P. D. and Fang, J. H. (1973) Crystal structures and mineral chemistry of hydrated

1077   ferric sulphates. III. The crystal structure of kornelite. American Mineralogist, 58, 535-

1078   539.

1079   Rosenzweig, A. and Gross, E. B. (1954) Goldichite, a new hydrous potassium ferric sulfate from

1080   the San Rafael swell, Utah. American Mineralogist, 40, 469-480.

1081   Ross, S. D. (1962) Forbidden transitions in the infra-red spectra of some tetrahedral anions – II.

1082   Sulphates. Spectrochimica, 18, 1575-1578.

1083   ___ (1974) Sulfates and other oxy-anions of Group VI. In V. C. Farmer, Ed., The Infrared

1084   Spectra of Minerals, 423-444. Mineralogical Society, London.

49

1085   Ruff, S. W., Christensen, P. R., Barbera, P. W., and Anderson, D. L. (1997) Quantitative thermal

1086   emission spectroscopy of minerals: A laboratory technique for measurement and

1087   calibration. Journal of Geophysical Research, 102, 14899-14913.

1088   Salisbury, J. W. and Eastes, J. W. (1985) The effect of particle size and porosity on spectral

1089   contrast in the mid-infrared. Icarus , 64, 586-588.

1090   ___ and A. Wald (1992) The role of volume scattering in reducing spectral contrast of

1091   reststrahlen bands in spectra of powdered minerals. Icarus , 96, 121-128.

1092   Sasaki, K., Tanaike, O., and Konno, H. (1998) Distinction of jarosite-group compounds by

1093   Raman spectroscopy. Canadian Mineralogist, 36, 1225-1235.

1094   Scordari, F., and Ventruti, G. (2009) Sideronatrite, $Na_2Fe(SO_4)_2(OH) \cdot 3 H_2O$: Crystal structure

1095   of the orthorhombic polytype and OD character analysis. American Mineralogist, 94,

1096   1679-1686.

1097   ___, ___, and Stasi, F. (2010) Metasideronatrite: Crystal structure and its relationship with

1098   sideronatrite. American Mineralogist, 95, 329-334.

1099   Sejkora, J. and Ďuda, R. (1998) Natroalunite and natrojarosite from Saca (Košice region,

1100   Slovakia). Mineralia Slovaca, 30, 315-320.

1101   Serna, C. J., Cortina, C. P., and Ramos, J. V. G. (1986) Infrared and Ramen study of alunite-

1102   jarosite compounds. Spectrochimica Acta, 42A, 729-834.

1103   Shokarev, M. M., Margulis, E. V., Vershinina, F. I., Beisekeeva, L. I., and Savchenko, L. A.

1104   (1972) Infrared spectra of iron (III) hydroxide sulphates and hydroxides. Journal of

1105   Inorganic Chemistry, 17(9), 1293-1296.

50

1106   Soptrajanov, B. and M. Trpkovska (1993) Copper sulfate monohydrate: Centrosymmetric or

1107   non-centrosymmetric? Journal of Molecular Structure, 293, 109-112.

1108   Steger, E. and Schmidt, W. (1964) Infrarotspektren von Sulfaten und Phosphaten. Berichte der

1109   Bunsengesellschaft für Physikalische Chemie, 68, 102-109.

1110   Strunz, H. and Nickel, E. (2001) Strunz Mineralogical Tables: Chemical Structural Mineral

1111   Classification System (9th edition), pp. 870. E. Schweizerbart'sche Verlagsbuchhandlung,

1112   Stuttgart.

1113   Süsse, P. (1967) Die kristallstruktur des botryogens. Naturwissenschaften, 54, 139-139.

1114   ___ (1968) The crystal structure of amarantite, $Fe_2(SO_4)_2O \cdot 7\ H_2O$. Zeitschrift für

1115   Kristallographie, 127, 261-275.

1116   Vassallo, A. M. and Finnie, K. S. (1992) Infrared emission spectroscopy of some sulfate

1117   minerals. Applied Spectroscopy, 46, 1477-1482.

1118   Ventruti, G., Stasi, F., and Scordari, F. (2010) Metasideronatrite: crystal structure and its relation

1119   with sidernatrite. American Mineralogist, 85, 329-334.

1120   Wang, A., Freeman, J. J., Jolliff, B. L., and Chou, I.-M. (2006) Sulfates on Mars: A systematic

1121   Raman spectroscopic study of hydration states of magnesium sulfates. Geochimica et

1122   Cosmochimica Acta, 70, 6118-6135.

1123   ___ and Ling, Z. C. (2011) Ferric sulfates on Mars: A combined mission data analysis of salty

1124   soils at Gusev crater and laboratory experimental investigations. Journal of Geophysical

1125   Research, 116, doi:10.1029/2010JE003665.

1126   ___, Bell III, J. F., Li, R., Johnson, J. R., Farrand, W. H., Cloutis, E. A., Arvidson, R. E.,

1127   Crumpler, L., Squyres, S. W., McLennan, S. M., Herkenhoff, K. E., Ruff, S. W.,

51

1128   Knudson, A. T., Chen, W., and Greenberger, R. (2008) Light-toned salty soils and

1129   coexisting Si-rich species discovered by the Mars Exploration Rover Spirit in Columbia

1130   Hills. Journal of Geophysical Research, 113, E12S40, doi:10.1029/2008JE003126.

1131 Wenrich, M. L. and Christensen, P. R. (1996) Optical constants of minerals derived from

1132   emission spectroscopy: Application to quartz. Journal of Geophysical Research, 101,

1133   15921-15931.

1134 Weitz, C. M., Noe Dobrea, E. Z., Lane, M. D., and Knudson A. (2012) Geologic relationships

1135   between gray hematite, sulfates, and clays in Capri Chasma. Journal of Geophysical

1136   Research, E00J09, doi:10.10292012JE004092.

1137 Wildner, M., and Giester, G. (1991) The crystal structures of kieserite-type compounds. I.

1138   Crystal structures of Me(II)$SO_4 \cdot H_2O$ (Me = Mn,Fe,Co,Ni,Zn). Neues Jahrbuch fur

1139   Mineralogie, Monatshefte, 1991, 296-306.

1140

1141 **Figure Captions**

1142 Figure 1: Pancam image of the bright soils in the *Spirit* rover tracks in Gusev Crater, Mars,

1143   indicating the presence of Fe sulfates in the subsurface of Mars. A broken, dragging

1144   wheel serendipitously exposed the yellowish/whitish minerals. Image credit:

1145   NASA/JPL/Cornell/Arizona State University

1146 Figure 2a: Mid-infrared thermal emissivity spectra of sulfates with finite clusters of SO_4

1147   tetrahedra and MX_6 octahedra, including their crystal structure diagrams -- coquimbite

1148   (Fang and Robinson 1970), römerite (Fanfani et al. 1970), and rozenite (Baur 1962).

1149   Band depths have been adjusted by multiplying the spectra by the parenthetical amounts;

1150   spectra are then offset for clarity.

52

1151   Figure 2b: VNIR reflectance spectra from 0.4-5 μm of sulfates with finite clusters of SO_4

1152   tetrahedra and MX_6 octahedra including coquimbite/paracoquimbite, römerite, and

1153   rozenite.

1154   Figure 3a: Mid-infrared thermal emissivity spectra of sulfates with chains of SO_4 tetrahedra and

1155 MX_6 octahedra, including amarantite, zincobotryogen, butlerite, parabutlerite,

1156   copiapite/ferricopiapite, magnesiocopiapite, and sideronatrite. In addition, the crystal

1157   structure diagrams are shown (amarantite from Süsse 1968; botryogen from Süsse 1967;

1158   butlerite from Fanfani et al. 1971; ferricopiapite from Fanfani et al. 1973; and

1159   metasideronatrite from Ventruti et al. 2010). Band depths have been adjusted by

1160   multiplying the spectra by the parenthetical amounts; spectra are then offset for clarity.

1161   Figure 3b,c,d,e: VNIR reflectance spectra of sulfates with chains of SO_4 tetrahedra and MX_6

1162   octahedra including b) amarantite, botryogen, butlerite and parabutlerite, c) copiapite

1163   from 0.4-5 μm, Mg-copiapite, and sideronatrite from 0.4-5 μm, d) three grain size

1164   fractions of amarantite from 0.3-2.65 μm, and e) three particle-size fractions of botryogen

1165   from 0.3-2.65 μm.

1166   Figure 4a: Mid-infrared thermal emissivity spectra of sulfates with sheets of $M_3(OH)_6(SO_4)_2$,

1167   including beaverite, hydronium jarosite, jarosite, and natrojarosite. In addition, the crystal

1168   structure diagrams for beaverite (Breidenstein et al. 1992) and jarosite (Basciano and

1169   Peterson 2007) are shown. Band depths have been adjusted by multiplying the spectra by

1170   the parenthetical amounts; spectra are then offset for clarity.

1171   Figure 4b: VNIR reflectance spectra from 0.4-5 μm of sulfates with sheets of $M_3(OH)_6(SO_4)_2$,

1172   including beaverite, jarosite, hydronium jarosite, and natrojarosite. The beaverite

1173   spectrum is offset for clarity.

53

1174   Figure 5a: Mid-infrared thermal emissivity spectra of sulfates with sheets of SO_4 tetrahedra and

1175 MX_6 octahedra, and their crystal structure diagrams -- including goldichite (Graeber and

1176   Rosenzweig 1971), kornelite (Robinson and Fang 1973), rhomboclase (Mereiter 1974),

1177   slavikite (Parafiniuk et al. 2010), and yavapaiite (Graeber and Rosenzweig 1971). Band

1178   depths have been adjusted by multiplying the spectra by the parenthetical amounts;

1179   spectra are then offset for clarity.

1180   Figure 5b: VNIR reflectance spectra from 0.4-5 μm of sulfates with sheets of SO_4 tetrahedra and

1181 MX_6 octahedra including rhomboclase, yavapaiite, slavikite, kornelite, and goldichite.

1182   The slavikite spectrum is offset for clarity.

1183   Figure 6a: Mid-infrared thermal emissivity spectra of sulfates with frameworks of SO_4 tetrahedra

1184   and MX_6 octahedra, and their crystal structure diagrams -- including szomolnokite

1185   (Wildner and Geister 1991) and voltaite (Mereiter 1972). Spectra are offset for clarity.

1186   Figure 6b: VNIR reflectance spectra from 0.4-5 μm of sulfates with frameworks of SO_4

1187   tetrahedra and MX_6 octahedra including szomolnokite and voltaite.

54

Table 1. Listing of the Fe-sulfate Minerals.

Mineral (XRD character)	Stoichiometric Composition	Sample and Character [a]	Locale
Amarantite (pure)	$Fe(SO_4)(OH) \cdot 3\,H_2O$	R6254-A ε ch; R <45 μm	Sierra Borda, Antofagasta, Chile; Collection of the Smithsonian - National Museum of Natural History
Beaverite (w/ ~5-7% anglesite)	$PbCu(Fe,Al)_2(SO_4)_2(OH)_6$	G1241 ε pellet; R <150 μm	Unknown
Botryogen-Zn	$(Zn,Mg,Mn)Fe(SO_4)_2(OH) \cdot 7\,H_2O$	C5525-3 ε ch; R <45 μm	Mina Quetena, Calama, Chile; Collection of the Smithsonian - National Museum of Natural History
Butlerite (w/ 5% parabutlerite)	$Fe(SO_4)(OH) \cdot 2\,H_2O$	VZO108 [b] ε pellet; R <45 μm	Borate, Calico Hills, San Bernardino, California
Copiapite [c] (w/ 25% ferricopiapite)	$FeFe_4(SO_4)_6(OH)_2 \cdot 20\,H_2O$	SPT125 ε ch; R <45 μm	Sierra Gorda, Chile; Collection of Ed Cloutis
Coquimbite [d]	$Fe_2(SO_4)_3 \cdot 9\,H_2O$	ML-S46 ε ch; R <125 μm	Alcaparrosa, Chile
Goldichite (pure)	$KFe(SO_4)_2 \cdot 4\,H_2O$	123922 ε ch; R <500 μm	Pozzuoli, Solfatara, Italy; Collection of the Smithsonian - National Museum of Natural History
Hydronium jarosite [e] (+ minor cation)	$(H_3O)Fe_3(SO_4)_2(OH)_6$	R10101 ε ch; R <45 μm	Boolcoomatta, South Australia, Australia; Collection of the Smithsonian - National Museum of Natural History
Jarosite (w/ trace unknown)	$KFe_3(SO_4)_2(OH)_6$	ML-S51 ε ch; R <45 μm	Copiapo Jarosite Mine, Dona Ana Co., NM
Kornelite [f] (pure)	$Fe_2(SO_4)_3 \cdot 7\,H_2O$	ML-S105 ε ch; R <45 μm	Synthesized by co-authors PLK and BCH
Magnesiocopiapite (pure)	$MgFe_4(SO_4)_6(OH)_2 \cdot 20\,H_2O$	ML-S86 ε pellet; R <45 μm	Alma Pyrite Mine, Leona Heights, Oakland, Alameda Co., CA
Natrojarosite (pure)	$NaFe_3(SO_4)_2(OH)_6$	95661 ε pellet; R 45-125 μm	Sunset Mining claim near Kingman, AZ
Parabutlerite (pure)	$Fe(SO_4)(OH) \cdot 2\,H_2O$	157716 ε ch; R <45 μm	Chiquicamata, Antofagasta, Chile; Collection of the Smithsonian - National Museum of Natural History
Rhomboclase (pure)	$(H_5O_2)Fe(SO_4)_2 \cdot 2\,H_2O$	ML-S85 ε ch; R <250 μm	Alcaparrosa, Chile
Römerite (pure)	$FeFe_2(SO_4)_4 \cdot 14\,H_2O$	R8415 ε >125 μm; R <45 μm	Near Skauriatissa, Island of Cyprus, Greece; Collection of the Smithsonian - National Museum of Natural History
Rozenite (pure)	$FeSO_4 \cdot 4\,H_2O$	JB626-B ε ch; R <125 μm	Iron Mountain, CA
Sideronatrite (+ minor phase)	$Na_2Fe(SO_4)_2(OH) \cdot 3\,H_2O$	115164 ε pellet; R <45 μm	Chiquicamata, Chile; Collection of the Smithsonian - National Museum of Natural History
Slavikite (pure)	$NaMg_2Fe_5(SO_4)_7(OH)_6 \cdot 33\,H_2O$	140229 ε pellet; R 45-125 μm	Valachov, Czech Rebublic; Collection of the Smithsonian - National Museum of Natural History
Szomolnokite (pure)	$FeSO_4 \cdot H_2O$	104276 ε ch; R <45 μm	Tintic Standard Mine, Dividend, UT; Collection of the Smithsonian - National Museum of Natural History

Voltaite (pure)	$K_2Fe_5Fe_3Al(SO_4)_{12} \cdot 18\ H_2O$	115035 ε ch; R <45 µm	United Verde Mine, Jerome, AZ; Collection of the Smithsonian - National Museum of Natural History
Yavapaiite (pure)	$KFe(SO_4)_2$	ML-S79 ε pellet; R <45 µm	Synthesized by Ferenc Forray (Babes-Bolyai U.)

[a] Character of sample where ch=chunk/chip(s) or pellet; otherwise particle size fraction is listed for measurements in emissivity (ε) or reflectivity (R)

[b] VNIR data used sample C5534 (Mina Quetena, Calama, Chile; XRD shows butlerite + minor other phase)

[c] Sample SPT125: Cloutis et al, 2006 identify this sample as 90% ferricopiapite/ 10% jarosite

[d] Sample ML-S46 contains subequal amounts of coquimbite and paracoquimbite

[e] Sample R10101 may contain have some cation substitution (e.g., K^+ or Na^+) for H_3O because the XRD peaks were shifted slightly from those of a hydronium jarosite reference endmember

[f] Sample ML-S105 spectrum was corrupted and data from $200 - 400\ cm^{-1}$ were lost

Table 2. Band Assignments of the Fundamental Vibrational Modes in Fe-sulfate Minerals (in cm^{-1}).

Mineral	δH_2O	ν_3	δOH	ν_1	H_2O libration	δOH	ν_4	γOH	ν_2	H_2O libration, M-O, or lattice
Amarantite	~1642	~1215 (sh) 1154 1090 1059	1018?	1004		804 ~748	~645 595 ~528		463	~289 trunc.
Beaverite	~1602	1163 1110 984?	1019	1001		~735	625 604 575		423	512 469 trunc.
Botryogen-Zn	~1660	1220 1164 (sh) 1132 1068 1031	1010	999		805	655 602 545 485		393?	280 trunc.
Butlerite	~1688	~1200 (sh) 1123 ~1045 (sh)	1013	992		806	694 657 592 506		441 ~413	252?/trunc.
Copiapite	~1662	~1212 ~1109 1047		998		~790	~603 ~542		~410	trunc.
Coquimbite	1690 (s)	1180 1100		1013		890 816	685 (s) 650 597		480 443	304 284 (sh) 278 252 (s) 247 218
Goldichite	~1640	1258 1169 1119		997		786	689 627 597		476 428	359 trunc.
Hydronium jarosite	~1651	1204 (s) 1121	1033	997?		898? 845? 760?	675 635		428 393	~526 475 ~336 ~265 or trunc.
Jarosite	1633	1220 1112	1020	1006			~662 (sh) 635		445	524 476 ~336 ~242?

Mineral										
Kornelite	~1665	1206 (sh) 1160 1121 1054		1020	751		650? 627 593		492? 448	No data below 400 cm^{-1}
Magnesio-copiapite	~1656	1213 1146 (sh) 1107 1049 1031? (sh)	1013	997			639 595 556		414	~262 or trunc.
Natrojarosite	~1635	1200 1107	1026	~1010			~666 632		441	524 478 347? 327 trunc.
Parabutlerite	~1688	1233 1176 1098 1054 1024	1013	997			650 602 503 ~476		446 ~330	256? trunc.
Rhomboclase	~1585	~1210 (sh) 1180 1068 (sh) 1043		1022		745	664 ~627	593	~485	308 trunc.
Romerite / roemerite	~1673	~1168 (sh) 1139 1078 1035		996	815?		~658 ~593		~477	trunc.
Rozenite	~1680	~1220 (sh) 1100 ~1013		992		818 ~760 735 ~692	~660 (sh) ~645 (sh) 602		~468	
Sideronatrite	~1637	1270 1217 1208 1139 1112 (sh) 1068 1034	see text	997			666 650 634 620 609 519	see text	409 400	308 ~265 trunc.
Slavikite[*]	~1612[‡]	1199 ~1084		~1000			597		462	trunc.

Szomolnokite		1226	1018	846		626	361?	trunc.
		1195				606		
		1149				554		
Voltaite	~1670‡	1171	1004		~832	671 (s)	439	251
		~1123 (sh)			(s)	625	375	
		1050			~735	584		
		979 (sh)?				520		
Yavapaiite		1254				676	469	370?
		~1142 (sh)				620	444	255
		1024				588	416?	

(s) Band is subtle.

(sh) Band occurs as a shoulder on a larger band.

trunc. Band is truncated, so band minimum is not known.

[*] Spectral quality is inferior.

[‡] Feature is very broad; position uncertain.

coquimbite/paracoquimbite (x 0.3)

römerite (x 1.8)

rozenite (x 1.2)

amarantite (x 1.7)

botroygen-Zn (x 0.7)

butlerite (x 0.8)

parabutlerite

copiapite/ferricopiapite (x 1.7)

magnesiocopiapite

sideronatrite (x 0.3)

Emissivity

Wavenumber (cm^{-1})

2000   1500   1000   500

1.0

0.8

0.6

0.4

0.2

0.0

-0.2

-0.4

beaverite

jarosite

beaverite (x1.2)

jarosite (x 0.5)

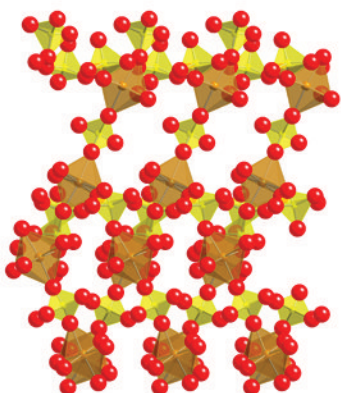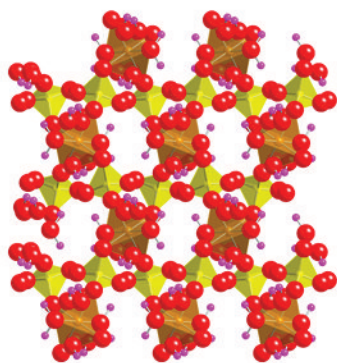hydronium jarosite (x 2.4)
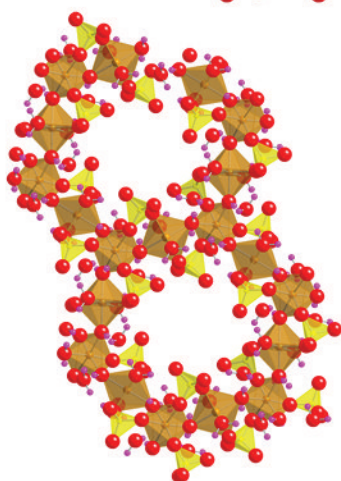
natrojarosite (x 0.4)

Emissivity

Wavenumber (cm⁻¹)
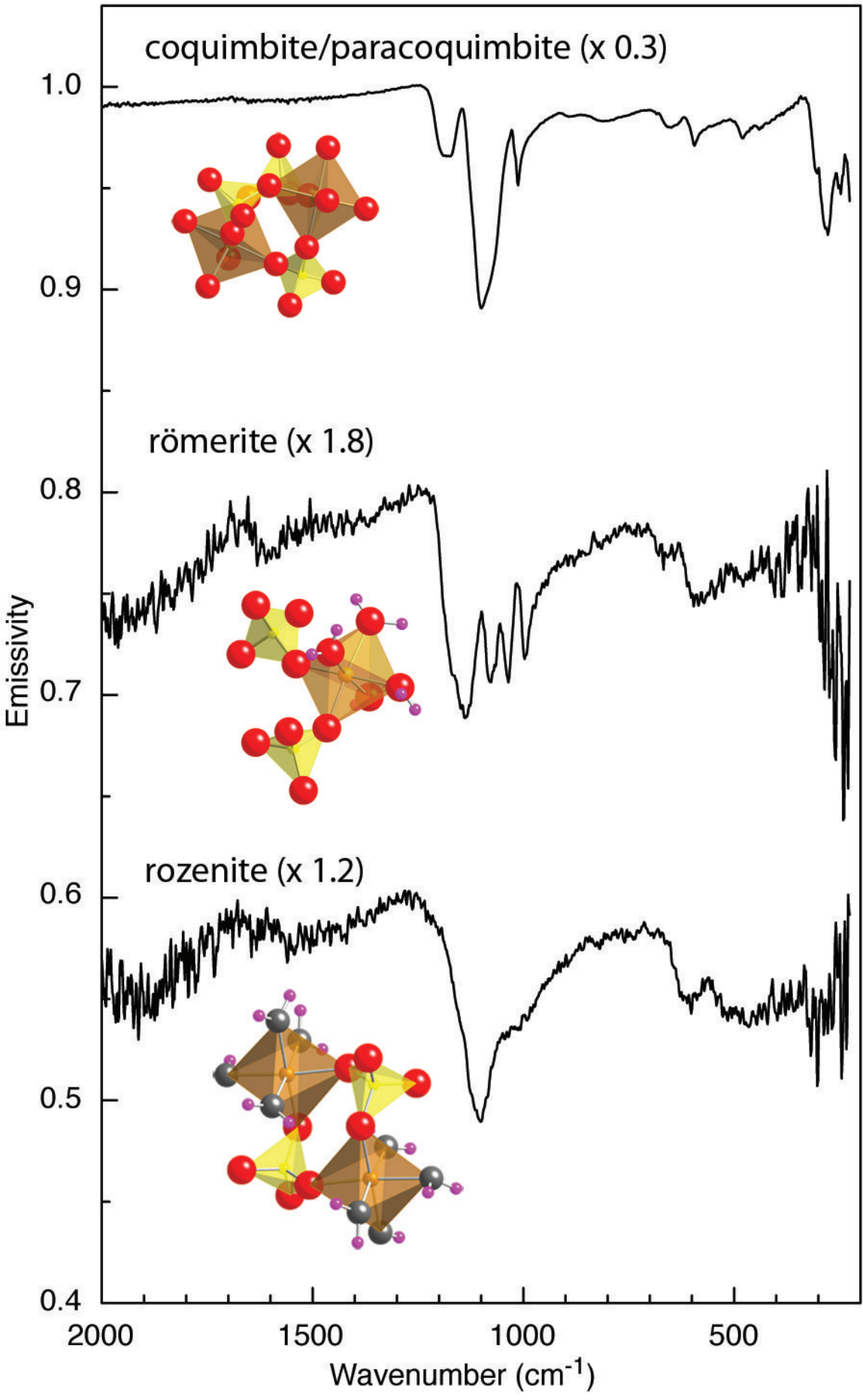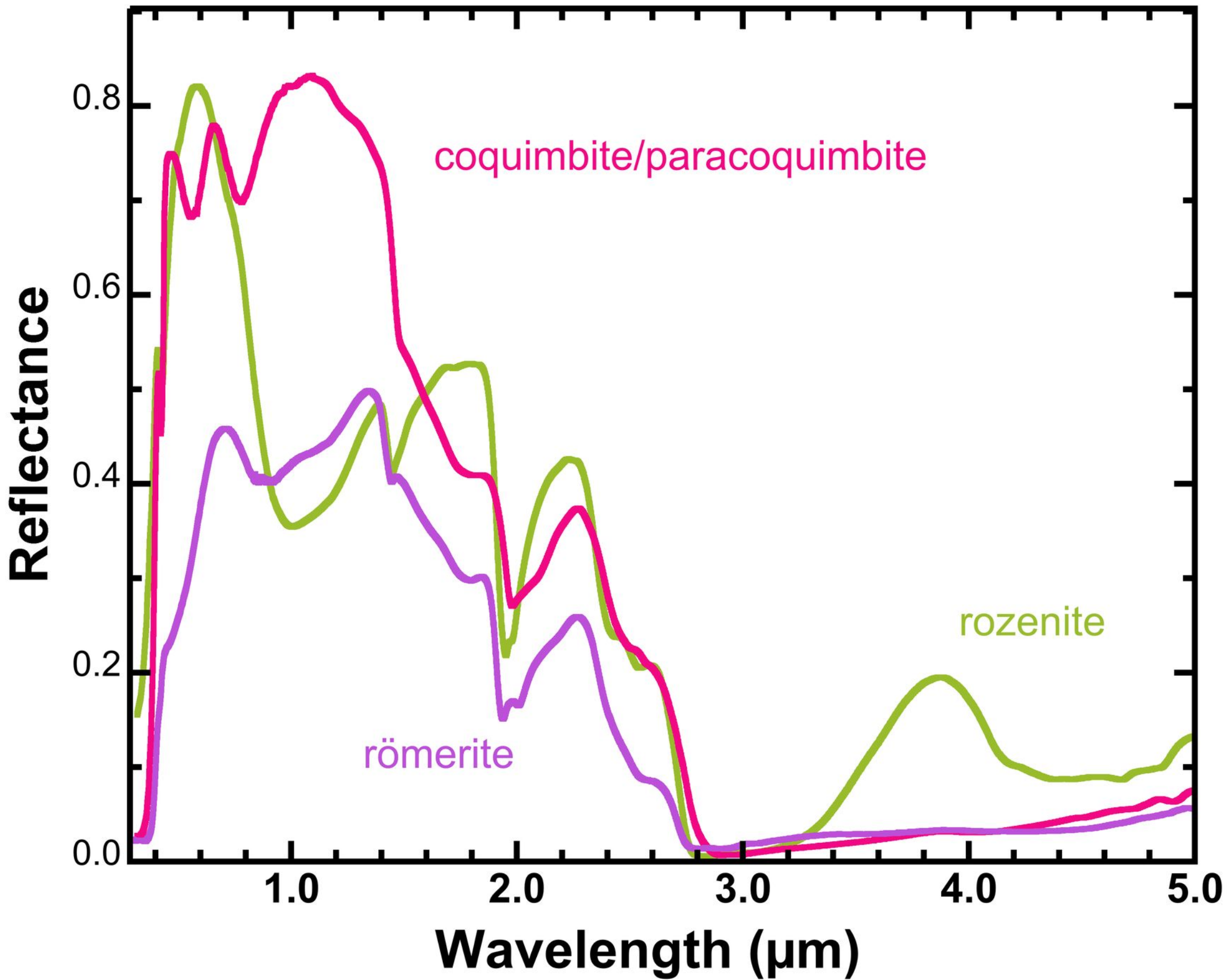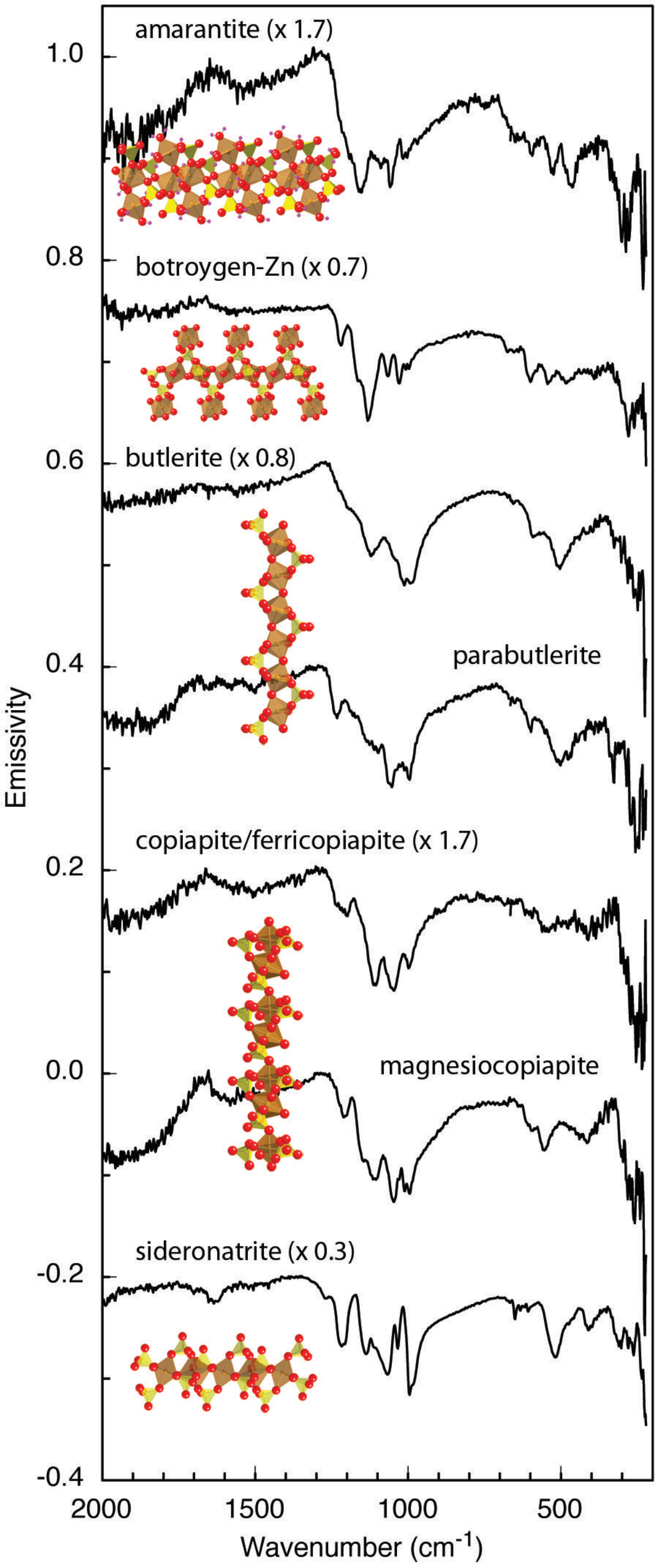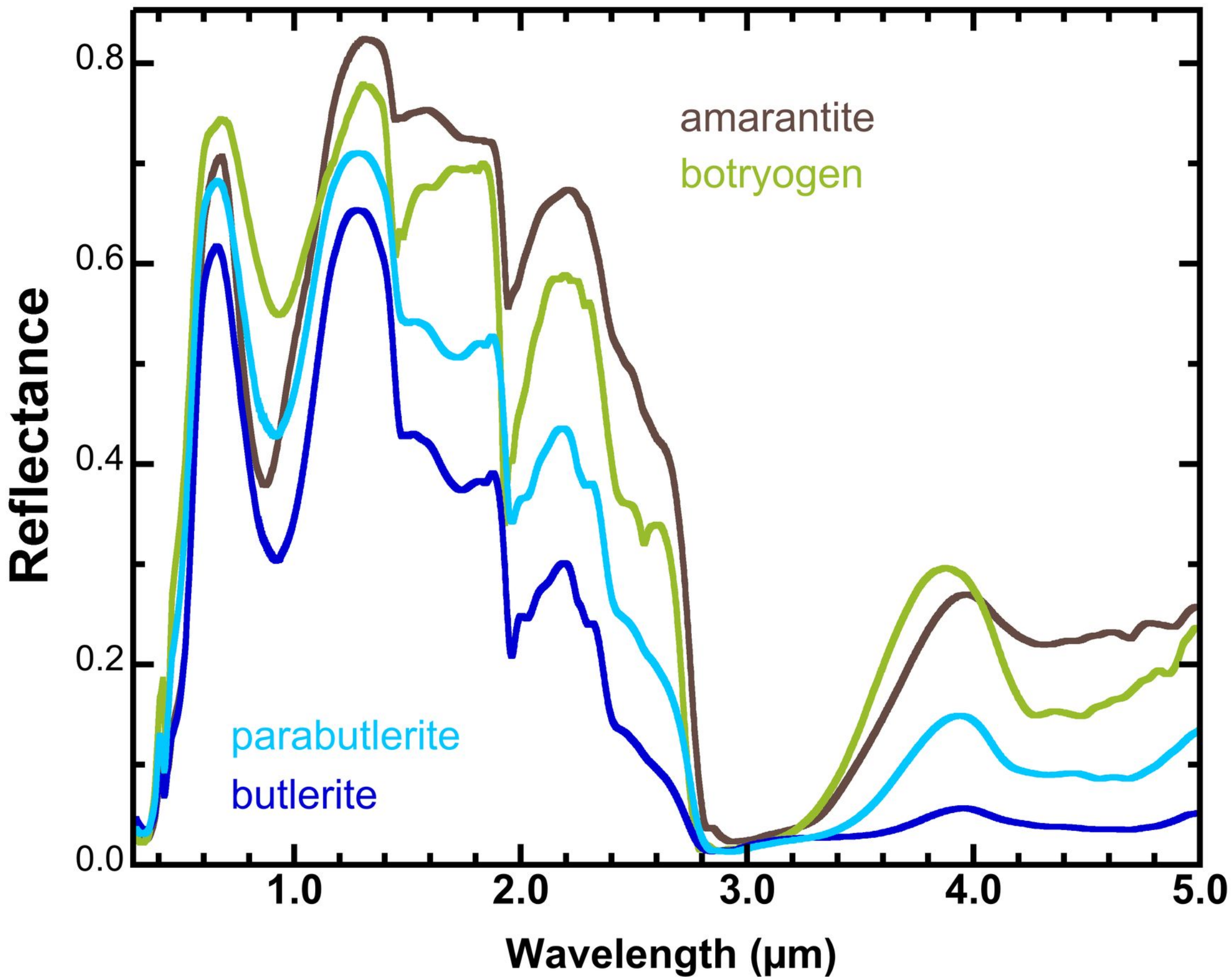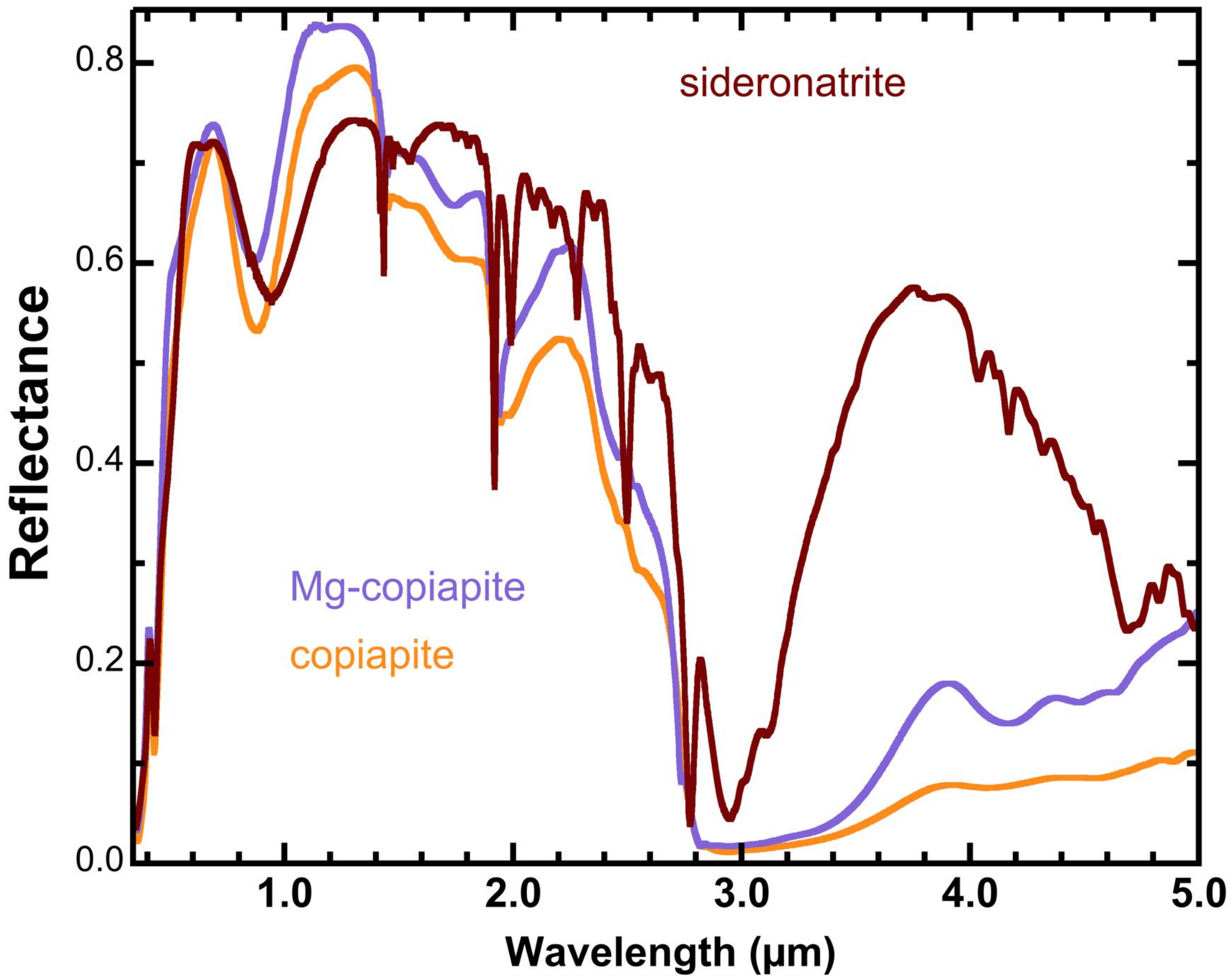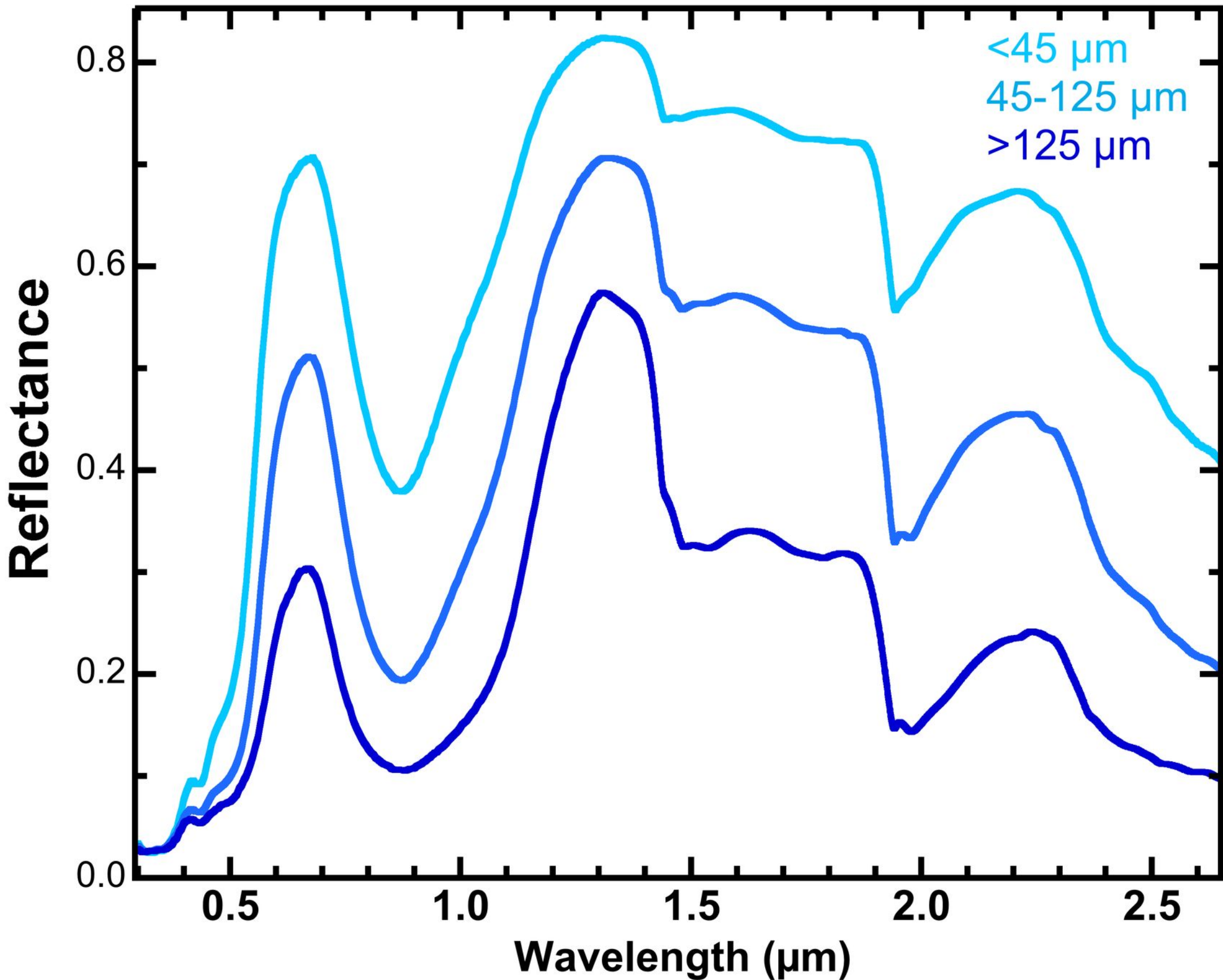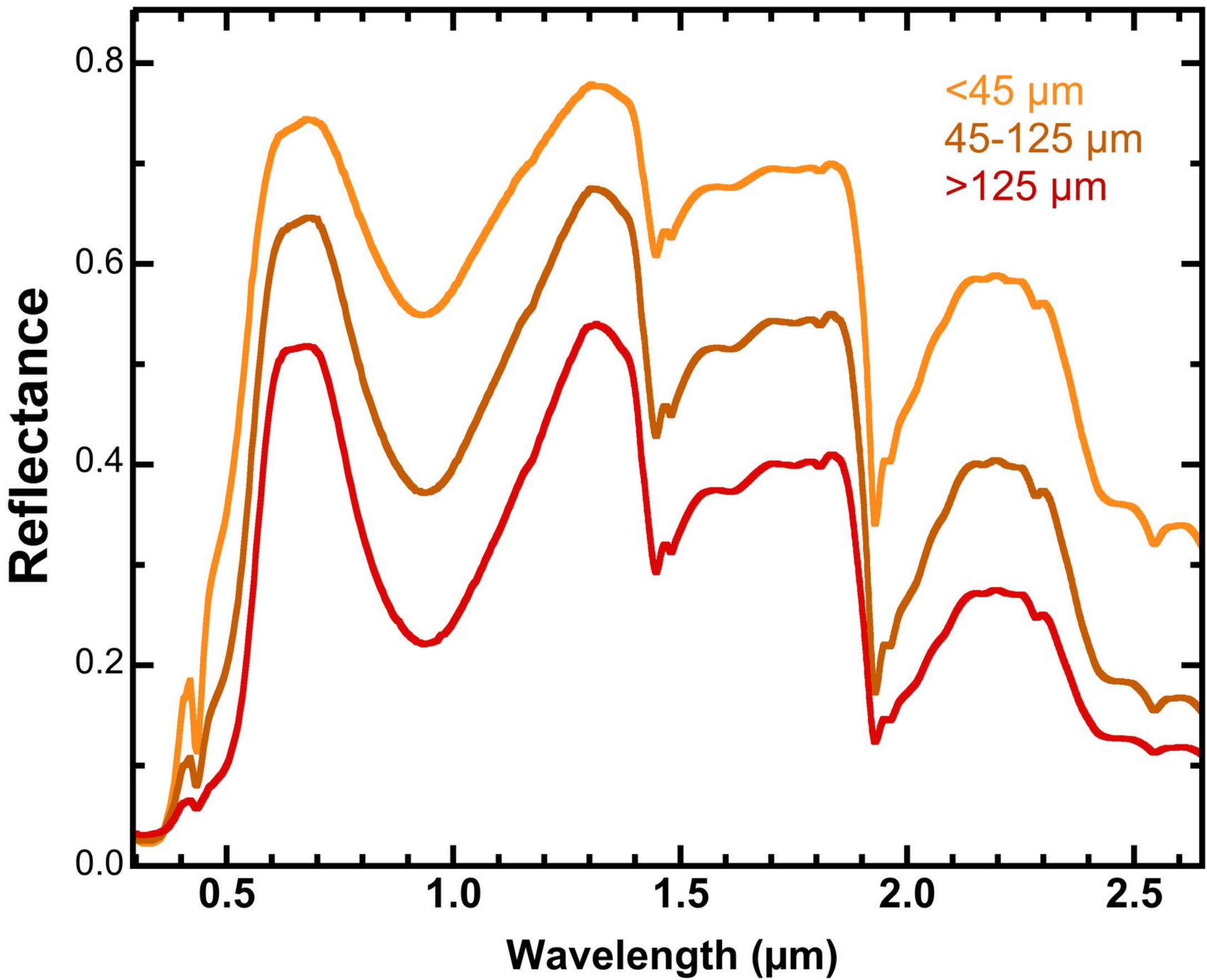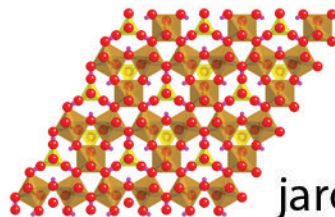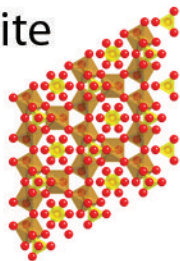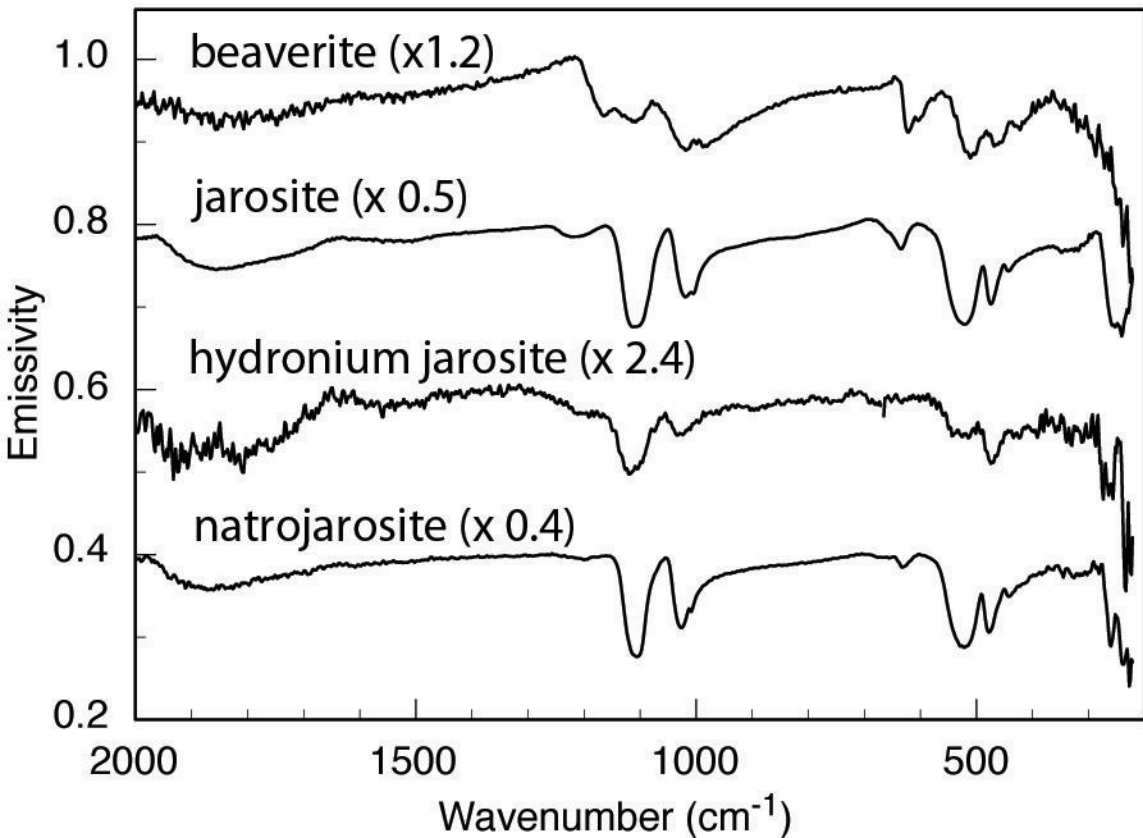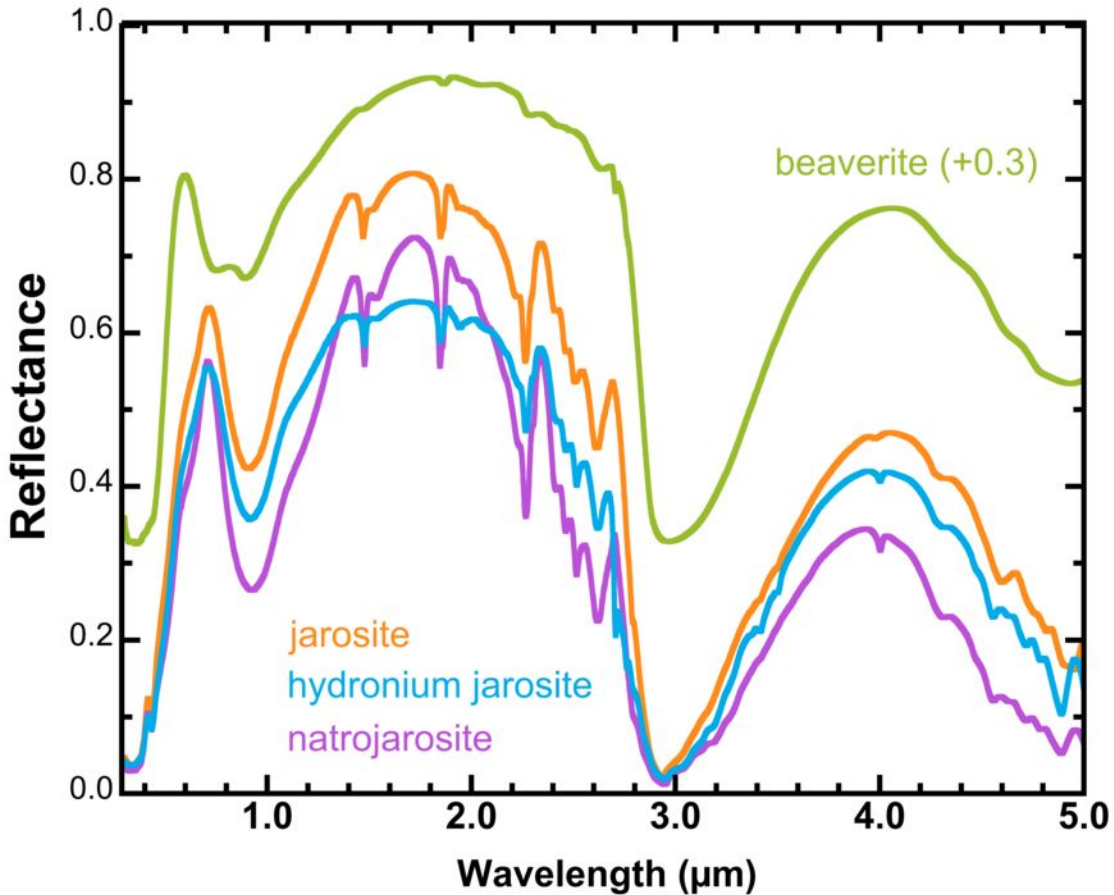
goldichite
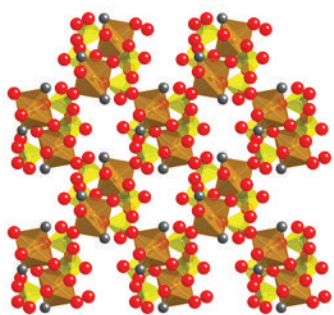
kornelite

rhomboclase

slavikite

yavapaiite

goldichite (x 1.2)

kornelite

rhomboclase (x 0.6)

slavikite (x 1.5)

yavapaiite (x 0.4)

Emissivity

2000   1500   1000   500

Wavenumber (cm⁻¹)